Polyphased brittle deformation around a crustal fault: a multi-scale approach based on remote sensing and field data on the mountains surrounding the Têt hydrothermal system (Eastern Pyrénées, France)

Audrey Taillefer, Gaétan Milesi, Roger Soliva, Loïs Monnier, Pauline Delorme, Laurent Guillou-Frottier, Elisabeth Le Goff

Polyphased brittle deformation around a crustal fault: a multi-scale approach based on remote sensing and field data on the mountains surrounding the Têt hydrothermal system (Eastern Pyrénées, France)

TAILLEFER Audrey[a*], MILESI Gaétan[b], SOLIVA Roger[c], MONNIER Loïs[d], DELORME Pauline[e], GUILLOU-FROTTIER Laurent[f], LE GOFF Elisabeth[g]

* *corresponding author*

[a*] Géosciences Montpellier, Univ Montpellier, CNRS, Univ Antilles, Montpellier, France. (+33) 6 50 60 16 64
audrey.taillefer@gmail.com

[b] Géosciences Montpellier, Univ Montpellier, CNRS, Univ Antilles, Montpellier, France.
gaetan.milesi@umontpellier.fr

[c] Géosciences Montpellier, Univ Montpellier, CNRS, Univ Antilles, Montpellier, France.
soliva@gm.univ-montp2.fr

[d] lois.monnier@yahoo.fr

[e] School of Geography and Environmental Science of Southampton, Highfield, Southampton SO17 1BJ, United Kingdom.
P.M.T.Delorme@soton.ac.uk

[f] BRGM, Georesources Division, 45060, Orléans, France ,
l.guillou-frottier@brgm.fr

[g] BRGM Direction territoriale Languedoc-Roussillon 1039 rue de Pinville 34000 Montpellier, France.
e.legoff@brgm.fr

Highlights

1. Geological features of adjacent mountains that allow the hydrothermal circulation.
2. The Têt fault system was formed during recent and polyphased tectonic stages.
3. Plio-Quaternary brittle faulting is widely distributed and reactivates oldest faults.
4. Fracture opening at depth are favored in crystalline rocks than in metasediments.
5. Fault intersections with background fracturing provide pathways for hydrothermal fluids.

Abstract

Studying hydrothermal systems in basement environments requires knowledge of fault and fracture network distributions. This study addresses this through multi-scale structural analysis of the Têt fault and its surrounding fracture systems (Eastern Pyrénées) using remote sensing and field data. This study aims to achieve this through: 1) precisely mapping and describing the brittle fault network, 2) analysing the distribution of lineaments and outcrop-scale fractures related to these faults, 3) making comparisons to fault-kinematic evidence combined in a new regional review, 4) examining the relations between fractures features and lithology, 5) applying statistical analysis to highlight relations between different scales of deformation. The complex fault network is inherited from consecutive tectonic stages (Hercynian, Pyrenean compression, Neogene extension) and has been reactivated since the middle-Miocene. NE–SW secondary faults are abundant at the regional scale, even away from the Têt fault. Major NW–SE faults are constituted by 10s-m wide brittle core zones, and NW–SE secondary faults are concentrated around the Têt fault, attesting that they had formed at shallow crust levels after the Oligo-Miocene extension. N–S fractures, formed during Pyrenean compression, are part of the background fracturing and are scattered throughout the study area. Intersections of fault and fracture networks provide efficient permeable pathways for meteoric and hydrothermal fluids. Finally, a dislocation model reveals a lithological control on fracture apertures in crystalline rocks, which appears more preserved at depth than in metasediments. All of these elements are integrated in a global model of the hydrothermal system establishment in accordance with the faulting sequence, with the damage distribution and with the lithology. This distributed fault system could represent the surface expression of the crustal thinning revealed by recent geophysical data. The realized identification of the lithological and structural characteristics of the surrounding mountains, allowing hydrothermal circulation to establish itself, provides a better understanding of the orogenic-belt related hydrothermal systems necessary to the geothermal exploration.

Keywords: fault, damage zone, fracture, hydrothermal, Pyrénées, remote sensing, hot spring, lithology, basement

1 Introduction

Orogenic-belt related hydrothermal systems (i.e. located in mountains, Moeck [2014]) are currently not targeted for geothermal exploitation, because of the complexities of this multi-factor environment. It is necessary to better identify the lithological and structural characteristics of the surrounding mountains, that allow hydrothermal circulation to establish itself. These systems are organized as follows. First, meteoric water infiltrates from recharge areas located on elevated surfaces. Then, under the effect of the topographic/pressure gradient, the water penetrates inside the massif and is heated at depth. Finally, hot hydrothermal fluids migrate toward the surface using pathways (i.e. fault damage zones and/or lithologic discontinuities) and emerge in the lower topographic areas, particularly in valleys [Forster and Smith, 1989; López and Smith, 1995; Curewitz and Karson, 1997; Magri et al., 2016; Taillefer et al., 2018]. The size of the hydrothermal cell depends on the distance between infiltration and emergence areas.

Faults involve a cataclastic impermeable core zone (CZ), surrounded by two permeable damage zones (DZ) constituted by highly fractured wall-rock [Caine et al., 1996; Wibberley et al., 2008; Faulkner et al., 2010; Bense et al., 2013]. Fracture density in DZ decreases with the distance from the fault, and is particularly enhanced at fault intersections and tips [Sanderson and Kim, 2005; Mitchell and Faulkner, 2009; Savage and Brodsky, 2011; Mayolle et al., 2019], where hot springs and recharge areas are preferentially localized [Curewitz and Karson, 1997; Faulds et al., 2010; Person et al., 2012; Taillefer et al., 2018; Schneeberger et al., 2018]. Finally, faults may juxtapose different lithologies, whose respective permeabilities control hot spring locations [Taillefer et al., 2017].

The way meteoric fluids infiltrate from the elevated areas adjacent to the hydrothermal systems is rarely studied because the size of hydrothermal cells reach km-dimensions between recharge and emergence areas (e.g., Bianchetti et al. [1992]). This requires the study of faults and fractures at a regional scale, that is challenging [Earnest and Boutt, 2014]. Fracture orientation, density, connectivity, and apertures, are critical factors to understand fluid circulation in basement rocks [Norton and Knapp, 1977; Sausse, 1998; Stober and

Bucher, 2007; Laubach et al., 2018]. Paleo and in-situ stress (tectonic, confining pressure, seismic activity) critically affects the permeability, in creating part of the fracture network, in controlling the fracture shapes and apertures [Sibson, 1987; Banks et al., 1996; Ingebritsen and Manning, 1999; Saar and Manga, 2004; Earnest and Boutt, 2014; Cox et al., 2015; Howald et al., 2015; Sanderson, 2016], and in cyclically re-opening or dissolving sealed (i.e. mineralized) joints and veins [Lowell et al., 1993; Mazurek, 2000; Géraud et al., 2006; Belgrano et al., 2016]. Both opening mode I and shear mode II and III fractures in normal and thrust fault system generally strike parallel to the main or secondary faults (e.g., Savage and Brodsky [2011] and Mayolle et al. [2019]). However, some of the mode I fractures can be observed normal to fault strike in the specific conditions where the horizontal maximum stress is very close to the horizontal minimum stress [Kattenhorn et al., 2000]. For strike-slip faulting, both opening mode and shear mode fracture orientation can be different than the main fault strike (e.g., Riedle structures in the in-plane dimension, Fossen [2016]) and stress perturbations can occur quite far from the main strike-slip fault (e.g., King et al. [1994] and Chéry et al. [2001]). Far from faults, background fracturing is related to rock deconfinement during uplift and erosion, i.e. exhumation, local topography or glacial unloading [Carlsson and Olsson, 1982; Augustinus, 1995; Clarke and Burbank, 2011; Earnest and Boutt, 2014; Jarman et al., 2014; Leith et al., 2014a,b]). Basement permeability could be there enhanced by several orders of magnitude [Aydin, 2000; Sonney and Vuataz, 2009; Cox et al., 2015]. How much of the background fracturing is tectonically generated, the distance over which faults influence the fracture pattern, and the stress field that maintain the fractures open, are key points to understand how permeability is distributed over infiltration areas, especially in areas with polyphased deformations.

The hydrothermal system of the Têt Valley (Eastern Pyrénées, France, Figure 1) is an orogenic-belt related hydrothermal system, where basement rock lithologies (gneisses, granites, metasediments) are deformed by both ductile shear zones and brittle faults resulting from a polyphase tectonic history (Hercynian and Pyrenean compression, Neogene extension). The link between the Neogene deformations [Calvet, 1999; Goula et al., 1999] and the thinning of the crust in the Eastern Pyrénées remain unclear and is currently discussed

[Mauffret et al., 2001; Nercessian et al., 2001; Gunnell et al., 2008; Chevrot et al., 2018; Diaz et al., 2018; Wehr et al., 2018; Canva et al., 2020; Jolivet et al., 2020]. Moreover, it is also unclear how meteoric water infiltrates deep enough to attain a temperature of 80 to 130°C [Taillefer et al., 2018]. Twenty-nine hot springs of this hydrothermal system (29 to 73°C) align along the major Têt fault, mainly in its footwall, near contacts between crystalline rocks and metasediments [Taillefer et al., 2017]. They are clustered into 4 main groups, from west to east: Llo, Saint-Thomas(-Prats-Balaguer), Thues(-Les-Bains), Vernet(-Les-Bains) (Figure 1). Meteoric waters are collected on recharge areas above 2000 ± 300 m of altitude, and are driven down to at least -3500 m where they warm under the effect of the geothermal gradient [Krimissa, 1995; Taillefer et al., 2018]. Hydrothermal fluids are then channeled by the Têt fault and NW–SE faults intersecting the topography [Taillefer et al., 2018]. This study site is therefore well-suited to analyze the distribution and features of a polyphased fracture network at a regional scale, and also to discuss its potential role for deep fluid infiltration. The diversity of fault orientations, tectonic phases and deformation processes allows to examine the recent and current stress-field, the deformation chronology, and the geodynamic context.

This study combines various approaches to highlight and quantify the deformation (i.e.faults, fractures, veins) at different scales (i.e. regional, secondary, outcrop). First, a review of the fault motions investigates the structural inheritance, reactivations, and recent or active tectonics. Subsequently, remote sensing interpretation of lineaments [Vignaroli et al., 2013; Meixner et al., 2018], i.e. secondary faults or fracture corridors [Gabrielsen and Braathen, 2014], coupled with fracture measurements at the outcrop-scale, allows characterisation of the fault network, the fracture patterns and their apertures. A simple dislocation numerical model based on linear elasticity allows estimating fracture aperture at depth, as a function of lithology (crystalline vs. metasediments) and confining pressure. Statistical analysis was also performed to examine the spatial distribution of strikes at different scales (major or secondary faults, outcrop scale fractures). All these elements contribute to a discussion of the regional tectonic context in regard to the documented deformation. In addition, a model of the hydrothermal system establishment along the Têt fault is presented.

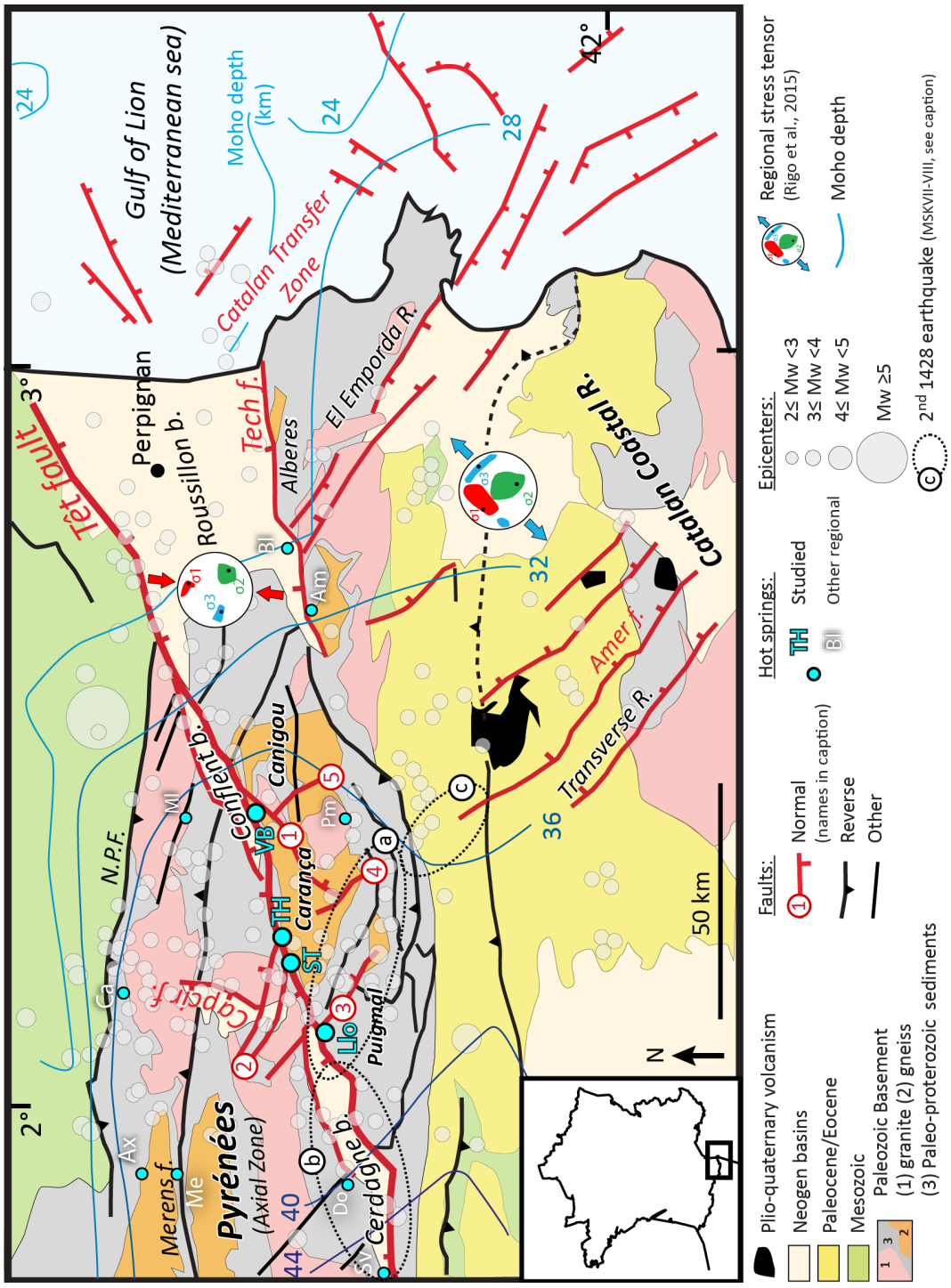

FIGURE 1: Structural sketch of Eastern Pyrénées. b.-basin ; f.-fault ; N.P.F.-North Pyrenean Fault. Normal faults: 1) Py, 2) Fontpedrouse, 3) Nuria, 4) Valter, 5) Parcigola. Hot springs: ST=St-Thomas-les-Bains-Prats-Balaguer, TH=Thues-les-Bains, VB=Vernet-les-Bains, Sv=Sant-Vincenc, Do=Dorres-Colomer, Me=Merens-Entre-Valls, Ax=Ax-les-Thermes, Ca=Carcanières, Ml=Molitg-les-Bains, Pm=Prats-de-Mollo-la-Preste, Am=Amélie-les-Bains, Bl=Le Boulou. Grey circle represent instrumental seismicity between 1989 and 1996, after Souriau and Pauchet [1998]. Possible locations of the 2^{nd} 1428 earthquake epicenter after a) Banda and Correig [1984], b) Briais et al. [1990], c) Olivera [2006], and Perea [2009]. The upper (respectively lower) regional stress tensor plot is for the northern (resp. southern) part of the map, the limits between these two domains is approximatively between the Paleozoic Basement of Pyrénées and the Tertiary foreland basins in Catalonia (see Rigo et al. [2015]). Isocontours of the Moho depth are modified from Goula et al. [1999], Mauffret et al. [2001] and Nercessian et al. [2001].

2 Review of Neogene tectonics in the Eastern Pyénées

2.1 Geological setting

Eastern Pyrénées relief is inherited from both the Eocene collision between the European and Iberic plates resulting in a doubly vergent orogeny [Choukroune et al., 1973; Roure et al., 1989], and from the Neogene extension and normal faulting resulting in the Gulf of Lion opening [Séranne, 1999; Maurel, 2003]. The study area is characterized by a progressive shallowing of the Moho from 45 km to 25 km from west to east (Figure 1, Mauffret et al. [2001], Nercessian et al. [2001],Gunnell et al. [2008], Chevrot et al. [2018], and Diaz et al. [2018]).

The hydrothermal system studied here is associated with the Têt fault, a major NE–SW normal fault that affects the central part of the Eastern Pyrenean range constituted of exhumed Hercynian basement (i.e. the "Axial Zone", Figure 1). In the study area, a Hercynian shear zone, the North Mylonitic Canigou Thrust (NMCT), juxtaposes Proterozoic and Paleozoic metasediments (schists with intercalated carbonate beds) with the gneissic dome of the Canigou-Carança. Both are intruded by late Hercynian granites, and crossed by numerous NW–SE to E–W normal ductile faults from the early Permian, filled by metric quartz veins [Casas, 1984; Guitard et al., 1992, 1998; Autran et al., 2005; Laumonier et al., 2015a,b, 2017]. The NMCT is crosscut by the Têt fault and crops out in its footwall. Pyrenean tectonic events are not well expressed in the study area, excepted for some local reactivation of Hercynian thrusts (e.g. the Merens, Llo, Vallespir and Canigou faults, McCaig and Miller [1986], Guitard et al. [1998], and Laumonier et al. [2017]) and pervasive extensional (mode I) N–S fracturing [Arthaud and Pistre, 1993].

The fault network is consequently inherited from Hercynian ductile deformation network mainly oriented NW–SE to E–W [Gourinard, 1971], and from Oligo-Miocene brittle deformations mainly oriented NE–SW to E–W. Similar fault orientations related to the Neogene extension are encountered south of the study area, in Catalonia, in the NW–SE normal faults of the Transverse Ranges and El Emporda, and through NE–SW offshore normal

faults along the coast (e.g., the Catalan Transfer Zone, Figure 1).

In addition, faults with N–S strikes (N010° to N030° and N150° to N180°) are also encountered over the study area (e.g., the Capcir fault), likely from the Plio-Quaternary period [Calvet, 1999; Briais et al., 1990], without clear evidence of the stress regime or tectonic events responsible from this deformation.

To summarize, the study area is indeed characterized by complex, polyphased, brittle tectonics from Paleogene to Neogene, especially for the recent period (see also Philip [2018]). In order to place the study area in this general context, Figure 2 compiles all data issued from the literature on fault kinematics from Paleogene to present, according to the orientations above presented (NW–SE, NE–SW and N–S). French Eastern Pyrénées and Catalonia are analysed separately, in agreement with the observations of Goula et al. [1999], Rigo et al. [2015], and Chevrot et al. [2011] on the current strain-rate (Figure 1, see Section 2.5). Details of fault motions and evidence from each publication are available in Supp. Mat. 1.

2.2 The NE–SW faults

NE–SW faults in the French Eastern Pyrénées and Catalonia have a Paleogene origin with compressive kinematics (reverse and strike-slip), as shown by outcrop arguments (stress-inversion, geomorphology, stratigraphy, see Cabrera et al. [1988] and Guimerà i Rosso [1988]), and deduced from exhumation rates issued from thermochronology data [Maurel, 2003; Maurel et al., 2008], that assumes the pre-existence of the Têt fault as a reverse fault.

The main activity of the NE–SW faults in the French Eastern Pyrenées (Têt and Tech faults and offshore faults, see Figure 1) is commonly linked to the Oligo-Miocene extensional episode. Numerous data show extensional activity in French Eastern Pyrénées starting at the Oligocene [Faillat et al., 1990; Roca and Desegaulx, 1992; Arthaud and Pistre, 1993; Medialdea et al., 1994; Tassone et al., 1994; Leclerc et al., 2001; Maurel et al., 2002; Maurel, 2003; Maurel et al., 2008; Milesi et al., 2019, 2020], and continuing during the Miocene [Clauzon, 1987; Rehault et al., 1987; Calvet, 1999; Mauffret et al., 2001; Babault, 2004; Lacan and Ortuño, 2012]. These normal motions are also observed at the south of Catalonia

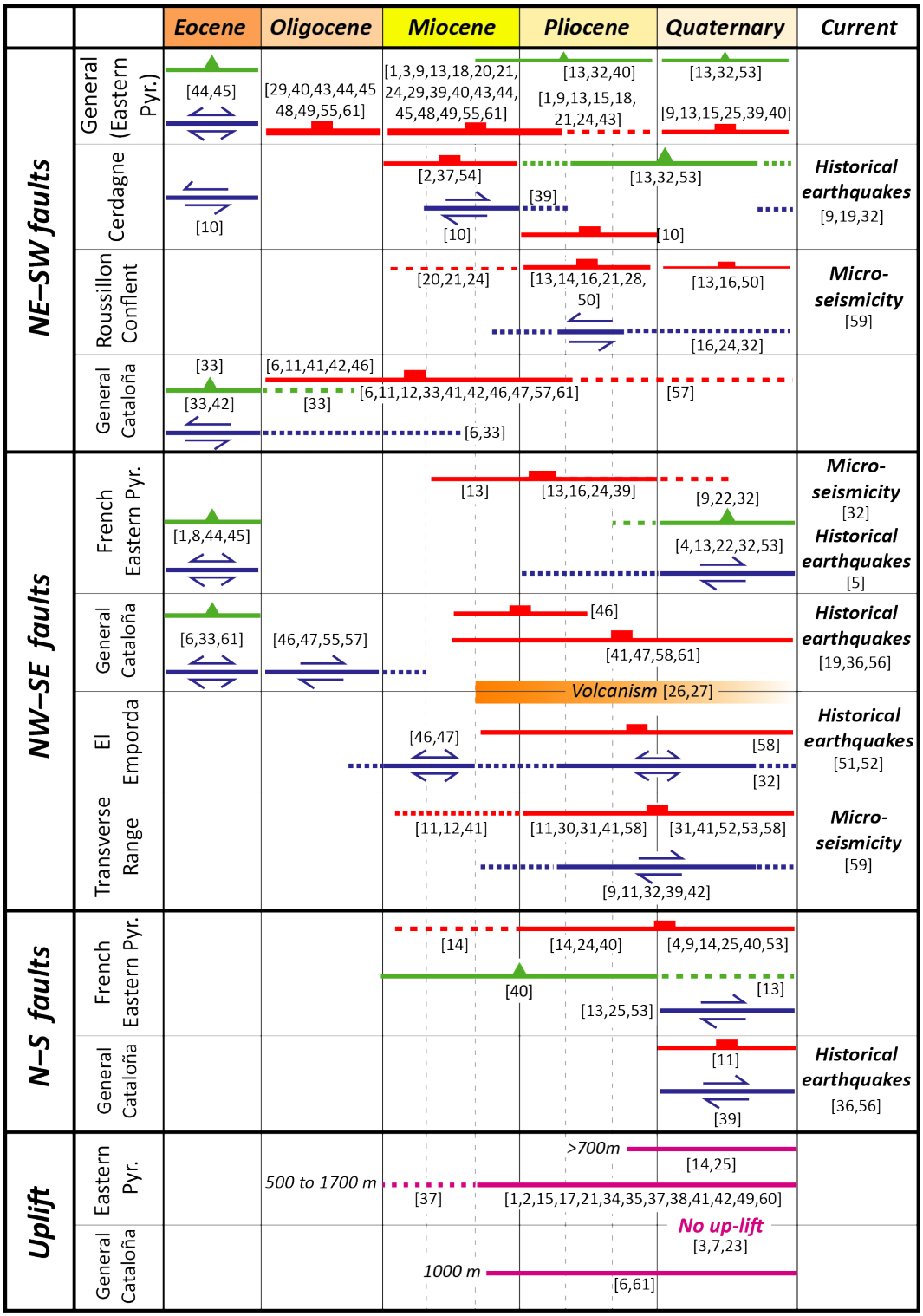

[1] Arthaud and Pistre, 1993 - [2] Augusti et al., 2006 - [3] Babault et al., 2004 - [4] Baize et al., 2002 - [5] Banda and Correig, 1984 - [6] Bartrina et al., 1992 - [7] Bosch et al., 2016 - [8] Bouchez et al., 1995 - [9] Briais et al., 1990 - [10] Cabréra et al., 1988 - [11] Cantarero et al., 2014 - [12] Cantarero et al., 2018 - [13] Calvet et al., 1999 - [14] Calvet et al., 2015 - [15] Calvet and Gunnell, 2008 - [16] Carozza and Baize, 2004 - [17] Carozza and Decaillau, 1999 - [18] Carozza and Decaillau, 2000 - [19] Chevrot et al., 2011 - [20] Clauzon, 1987 - [21] Clauzon et al., 2015 - [22] Cointre, 1987 - [23] Curry et al., 2019 - [24] Delcaillau et al., 2004 - [25] Delmas et al., 2018 - [26] Donville, 1937a - [27] Donville, 1937b - [28] Duvail et al., 2005 - [29] Faillat et al., 1990 - [30] Fleta et al., 2001 - [31] Gimenez et al., 1996 - [32] Goula et al., 1999 - [33] Guimera, 1984 - [34] Gunnell et al., 2008 - [35] Gunnell et al., 2009 - [36] Herraiz et al, 2000 - [37] Huyghe et al., 2020 - [38] Jarman et al., 2014 - [39] Lacan and Ortuno, 2012 - [40] Leclerc, 2000 - [41] Lewis et al., 2000 - [42] Mauffret et al., 2001 - [43] Maurel et al., 2002 - [44] Maurel, 2003 - [45] Maurel et al., 2008 - [46] Medialdea et al., 1996 - [47] Medialdea et al., 1996 - [48] Milesi et al., 2019 - [49] Milesi et al., 2020 - [50] Oele et al., 1963 - [51] Oliviera et al., 2006 - [52] Perea, 2009 - [53] Philip et al., 1992 - [54] Pous et al., 1986 - [55] Rehault et al., 1983 - [56] Rigo et al., 2015 - [57] Roca and Desegaulx, 1992 - [58] Saula et al., 1994 - [59] Souriau and Pauchet, 1998 - [60] Suc and Fauquette, 2012 - [61] Tassone et al., 1999

FIGURE 2: Synthesis of the fault kinematics in global Eastern Pyrénées during Neogene issue from evidence in the literature. Lines represent fault motions: normal (red), reverse (green), and strike-slip (blue, arrows for kinematics). Details of fault motions and evidence for each publication are available in Supp. Mat. 1.

from the Coastal Ranges to the Valencia Basin [Guimerà i Rosso, 1988; Lewis et al., 2000; Cantarero et al., 2014, 2018] and at the north in the Languedoc forming the Gulf of Lion [Séranne et al., 1995; Séranne, 1999].

However, the activity of these faults since the end of the Miocene and during the Plio-Quaternary period seems more complex: the observed recent displacements are only of 100s of meters [Roca and Desegaulx, 1992; Tassone et al., 1994; Calvet, 1999; Carozza and Delcaillau, 2000; Carozza and Baize, 2004; Delcaillau et al., 2004; Maurel et al., 2008; Lacan and Ortuño, 2012], and the rare kinematic and stress evidence varies over the area [Goula et al., 1999; Lacan and Ortuño, 2012; Rigo et al., 2015].

The Têt fault is the main NE–SW fault in the study area. This 80 km long brittle fault extends down at least through the upper crust [Chevrot et al., 2018; Diaz et al., 2018] and was formed during two main extensional phases. The first stage, from late Oligocene to early Miocene, corresponds to the initiation and main faulting (∼2000 m offset) of the Têt fault, and the formation of the Canigou-Carança ranges in its footwall [Roca and Desegaulx, 1992; Tassone et al., 1994; Mauffret et al., 2001; Maurel, 2003; Delcaillau et al., 2004; Maurel et al., 2008]. According to Mauffret et al. [2001], most of the normal motions along onshore and offshore NE–SW faults occurred during the Miocene to early Pliocene period: 1.7 km uplift is estimated in the offshore part of the Albères range, south east of the area (Figure 1).

Usually, middle-Miocene to late Pliocene is commonly associated to a second stage as a reactivation stage with more modest normal displacements (150 – 500 m, Pous et al. [1986], Clauzon [1987], Rehault et al. [1987], Roca and Desegaulx [1992], Tassone et al. [1994], Calvet [1999], Leclerc et al. [2001], Carozza and Baize [2004], Delcaillau et al. [2004], Agustí et al. [2006], Clauzon et al. [2015], and Huyghe et al. [2020]). However, there is also evidence of 1–2 km vertical displacements for the Canigou and Alberes ranges (Figure 1), on the basis of the deposit petrography in the basins and implications in terms of relief denudation [Calvet, 1996; Calvet et al., 2008]. However this second stage is not recorded by thermochronological study [Maurel, 2003]. Most of the evidence describes a continuity of normal motions during the Pliocene [Oele et al., 1963; Clauzon, 1987; Rehault et al., 1987; Cabrera et al., 1988;

Calvet, 1999; Carozza and Delcaillau, 1999, 2000; Leclerc et al., 2001; Delcaillau et al., 2004; Duvail et al., 2005; Calvet et al., 2008; Clauzon et al., 2015].

Various studies show a diachrony between the western (i.e. Cerdagne) and eastern (i.e. Conflent and Roussillon) segments of the Têt fault (Figure 1). Since the end of Miocene, the extension recorded in Cerdagne is accommodated by normal [Pous et al., 1986; Agustí et al., 2006] to right-lateral slip [Cabrera et al., 1988], allowing the pull-apart opening of the basin. Geomorphological evidence of normal motions from Pliocene to middle Quaternary have been found exclusively in Cerdagne [Calvet, 1999]. Additionally, reverse and strike-slip faults affect Quaternary sediments of the Cerdagne basin [Philip et al., 1992; Goula et al., 1999]. The Rousillon basin formation extend from Oligocene to lower Miocene [Calvet, 1996; Maurel et al., 2002; Calvet et al., 2008]. Normal faults affect Pliocene sediments in Conflent [Oele et al., 1963; Leclerc et al., 2001; Calvet et al., 2014] and potentially more recent offshore sediments [Roca and Desegaulx, 1992]. Tectonic evidence show post-Miocene reverse motions on basins both in Cerdagne (post-Messinian) and west of Roussillon (post-lower-Pliocene, Goula et al. [1999], Leclerc et al. [2001]).

The major normal activity of the NE–SW faults in the French Eastern Pyrénées appears to finish at the end of Pliocene [Mauffret et al., 2001; Delcaillau et al., 2004; Maurel et al., 2008]. However, triangular facets along the Têt, Py, and Tech fault scarps are interpreted as marker for normal motions during the Quaternary [Briais et al., 1990; Calvet, 1999]. Petit and Mouthereau [2012] suggest that the triangular facets along the Têt fault are formed by differential erosion of the Hercynian mylonite. However, facets on scarps where mylonites are not present remain unexplained (Cerdagne segment of the Têt fault, Py and Capcir faults, Delmas et al. [2018]). Many authors agree that if Quaternary normal displacements exist, they are low (<300 m, Oele et al. [1963], Calvet [1999], Carozza and Delcaillau [2000], Leclerc et al. [2001], Maurel [2003], Delcaillau et al. [2004], Duvail et al. [2005], Maurel et al. [2008], and Lacan and Ortuño [2012]), and could be the partial result of exhumation processes [Carozza and Baize, 2004]. Extensional activity along the NE–SW faults in Catalonia appears more regular during the Oligo-Miocene [Guimerà i Rosso, 1988; Roca and Desegaulx, 1992; Tassone et al., 1994; Lewis et al., 2000; Mauffret et al., 2001; Cantarero et al., 2014, 2018].

Moderate present-day seismicity, with magnitudes ranging from 2 to 4, is observed in the area (Goula et al. [1999] and Rigo et al. [2015], Figure 1) with an possible alignment of hypocenters along the NE part of the Têt fault [Souriau and Pauchet, 1998]. However, evidence of a recent or current tectonic activity in Cerdagne such as the 1970 earthquake [Goula et al., 1999], or the possible location of the 1427-1428 historical earthquake (Briais et al. [1990], Figure 1) are the only evidence for neotectonic activity in this otherwise seismically quiet segment of the Têt fault [Souriau and Pauchet, 1998].

2.3 The NW–SE faults

Numerous NW–SE faults in the French Eastern Pyrenées Axial Zone are described as ductile inherited regional faults in geological maps and handbooks [Guitard et al., 1992, 1998; Autran et al., 2005; Laumonier et al., 2015a,b, 2017] or as secondary faults (i.e. 100s of meters scale). Their brittle component and recent kinematics have received little attention [Gourinard, 1971], in comparison to similarly oriented faults in North-Catalan Ranges (El Emporda and Transverse Range, Figures 1 and 2). However, these faults are of particular importance, because hot springs commonly localize at their intersection with the Têt fault, and also along them outside of the study area (e.g., Merens-entre-Valls, Dorres-Colomer, Ax-les-Thermes, Molitg-les-Bains, see Figure 1).

In the study area, numerous faults with these strikes are late Hercynian (early Permian), often filled by 10s-m wide quartz veins [Guitard et al., 1992, 1998; Autran et al., 2005; Laumonier et al., 2015a,b, 2017]. Late-Hercynian dextral offset affects the Mont-Louis granite [Bouchez and Gleizes, 1995; Autran et al., 2005]. Maurel [2003] and Maurel et al. [2008] propose that these faults may have been reactivated during the Pyrenean compression, as for the similarly oriented fault of Merens, north of the study area [McCaig and Miller, 1986]. This fault, as well as the NW–SE faults in Cerdagne, has been reactivated as a normal fault during the Quaternary [Gourinard, 1971; Turu and Planas, 2005].

After Cabrera et al. [1988], normal movements on NW–SE faults and the Têt fault participate in the transtensive opening of the Cerdagne basin at the end of Miocene. Evidence

of reverse to right-lateral motions on NW–SE faults may affect the Plio-Quaternary series [Cointre, 1987; Philip et al., 1992; Calvet, 1999; Goula et al., 1999; Delcaillau et al., 2004]. Finally, reverse focal mechanisms are observed on faults with these orientations inside the Caranca range by Goula et al. [1999] and north of the Cerdagne basin [Chevrot et al., 2011], and extensional focal mechanisms south of the Puigmal range by Chevrot et al. [2011].

The NW–SE faults that give structure to the El Emporda and Transverse ranges (Figure 1) are interpreted as normal listric faults recording up to 1000 m of offset [Philip et al., 1992; Saula et al., 1994]. Strike-slip movements along these faults have been recorded during the Paleogene and Oligocene periods [Rehault et al., 1987; Guimerà i Rosso, 1988; Bartrina et al., 1992; Roca and Desegaulx, 1992; Tassone et al., 1994; Mauffret et al., 2001]. On these faults, normal kinematics start during the Miocene [Tassone et al., 1994]. They are mainly active from upper Miocene to Quaternary in El Emporda basin, and from upper Pliocene to Quaternary in the Transverse ranges [Medialdea et al., 1994; Saula et al., 1994; Lewis et al., 2000], although the activity decreases during Pliocene [Tassone et al., 1994]. They localize volcanism from Tortonian to Quaternary [Donville, 1973a,b]. The offshore equivalent of these faults (Catalan Transfer Zone) are interpreted as transfer faults with right-lateral motions between the upper Oligocene and lower Miocene [Mauffret et al., 2001; Nercessian et al., 2001], induced by a transient contraction phase during the lower Miocene [Roca and Desegaulx, 1992]. Geomorphological evidence (triangular facets, drainage system) suggest that some of these faults have been reactivated with normal and right-lateral motions during the Plio-Quaternary period [Briais et al., 1990; Calvet, 1999; Mauffret et al., 2001; Lacan and Ortuño, 2012; Cantarero et al., 2014], as highlighted by seismic activity [Souriau and Pauchet, 1998; Goula et al., 1999; Chevrot et al., 2011], including the potential location of the 1427-1428 earthquakes (Banda and Correig [1984], Olivera [2006], and Perea [2009], see Figure 1).

2.4 N–S faults

Kinematic evidence for N–S faults in the study are rare. In French Pyrénées, some of these faults are large (e.g., the Parcigola fault, Laumonier et al. [2015a]) and/or associated with Neogene basin as the Capcir fault (Figure 1). They mainly show evidence for normal motions with a dextral tendency for the NNE and NNW faults since the Miocene [Briais et al., 1990; Philip et al., 1992; Calvet, 1999; Goula et al., 1999], as highlighted by the fault scarp and the down-thrown basin of the Capcir fault. Locally, 100s-m long N–S faults are marked by reverse slickensides in Plio-Quaternary sediments [Calvet, 1999; Leclerc et al., 2001; Baize et al., 2002].

In Catalonia, the general strike of some faults (e.g., Amer, Albanya) is close to N–S. As in French Eastern Pyrénées, structural evidence indicates that these faults have experienced mainly main normal motions with dextral tendency [Fleta et al., 2001; Lacan and Ortuño, 2012; Cantarero et al., 2014]. This recent activity is highlighted by historical earthquakes [Banda and Correig, 1984; Goula et al., 1999; Olivera, 2006; Rigo et al., 2015].

2.5 The current uplift and present-day tectonics

Based on thermochronology, geomorphology, isotopy and numerical models, uplift of the entire Eastern Pyrénées is suspected to have occurred since 10 Ma [Bartrina et al., 1992; Tassone et al., 1994; Augustinus, 1995; Carozza and Delcaillau, 1999; Lewis et al., 2000; Calvet et al., 2008; Gunnell et al., 2008, 2009; Suc and Fauquette, 2012; Calvet et al., 2014; Jarman et al., 2014; Clauzon et al., 2015; Huyghe et al., 2020; Milesi et al., 2020]. The extend of this potential uplift is debated (between 500 and 1700 m), the timing is rather well constrained, with a possible acceleration during the Quaternary [Calvet et al., 2014; Delmas et al., 2018]. However, geomorphological arguments [Babault, 2004; Bosch et al., 2016] and numerical models [Curry et al., 2019] have also been put forward to contend that there is no general uplift, but mass transfers from the range into adjacent basins. Interestingly, the start of this uplift corresponds to the time at which there is no more consensus about the

fault motions, for all fault strikes (Figure 2).

Numerous previous study exist about the current stress field in the study area [Cointre, 1987; Philip et al., 1992; Goula et al., 1999; Leclerc et al., 2001; Delcaillau et al., 2004; Lacan and Ortuño, 2012; Rigo et al., 2015]. Considering the previous observations, they suggest that the general tectonic regime has changed during the Pliocene from extensional to contractional. The stress tensor is either strike-slip or reverse, with a maximum horizontal compression oriented NE–SW to N–S (see Supp. Mat. 1). Rigo et al. [2015] separate the French Eastern Pyrénées of Catalonia as we do, based on the results of stress tensors derived from seismic data inversion (see Figure 1). The French Eastern Pyrénées would be currently under a N–S compression: N–S compressive or E–W extensional in Cerdagne, NW–SE transtensive in the central part of the study area, and N–S compressive in Conflent/Roussillon. Catolonia would undergo a general NE–SW to E–W extension with large uncertainties. The whole Eastern Pyrénées would undergo a general extensional regime [Chevrot et al., 2018].

In brief, the complex fault network over the study area is inherited from at least three main tectonic stages (Hercynian and Pyrenean compression, and Oligo-Miocene extension), and has been reactivated since the Pliocene by a transient and laterally varying stress field. It is still not clear when the NW–SE and N–S faults, and associated deformations, have been reactivated or created, a question that will be addressed in the following sections. Processes that could explain these complex fault patterns and kinematics and the recent stress-field, will be addressed in the discussion, accounting for the new data provided below.

3 Methods

3.1 Remote sensing

We combine geological maps [Llac et al., 1988; Llac, 1989; Guitard et al., 1992, 1998; Autran et al., 2005; Laumonier et al., 2015a,b, 2017], SPOT 6-7 panchromatic satellite images (1.5 m, Système Pour l'Observation de la Terre) and aerial pictures (5 m) from IGN=Institut Geographique National (French geographical survey), and digital elevation

model (DEM, USGS GT30W020N90, 30 m) with QGIS3.10 software in order to trace faults and lineaments. Because main Neogene brittle faults are characterized by geomorphological features (relief, triangular facets and basins, Yeats et al. [1997]), fault mapping is mainly derived from topographic ruptures observed in the DEM. Smaller fault patterns or fracture corridors (i.e. immature faults) are identified using lineament mapping on satellite and aerial images. Major fault mapping is confirmed and completed by fieldwork.

Lineament refers to any visible straight line at the Earth surface corresponding to a geological or geomorphological object [Clark and Wilson, 1994]. They appear as linear pixel color anomalies corresponding to variations of field features (Jordan and Schott [2005], see an example of mapping in Supp. Mat. 2). The vegetation cover map (OCEGE from IGN), available in Supp. Mat. 2, indicates that 45 % of the analyzed surface is covered by intense vegetation or recent sediment deposits. Rare lineaments in areas covered by sediments will be discussed in regard to the recent deformations. However, high lineament density is encountered in forested areas as well as in grasslands or barren areas, suggesting a limited detection bias. The manual interpretation of lineaments allows geological and anthropogenic lineaments to be distinguished, with a good reproducibility and with different manual operators [Sander et al., 1997]. Distance between the Têt fault and lineaments or fracture measurement stations is automatically calculated using the NNjoin plug in QGIS3.10. (data of lineaments and distance to the Têt fault are available in Supp. Mat. 2) Representativity of lineament populations grouped by strike (i.e. NE–SW, NW–SE, N–S) was validated by statistical analysis detailed below. The ratio of a group of lineaments (e.g., NE–SW, NW–SE) compared to the Têt fault distance is realized by counting the amount of lineaments of the considered group, and the total amount of lineaments, comprising within the following 26 ranges of distance (in m): 0–100, 100–200, 200–500, (500 ;500 ;3000), (3000 ;1000 ;21000).

3.2 Field data

A field campaign allowed faults and fractures to be identified and measured at a range scale, and to check the validity and the nature of remotely sensed lineaments (see location

map of measurements in Supp. Mat. 4). Joints without mineral infills or coatings are considered as fractures without evidence for shearing (mode I) allowing them to be differentiated from shear-related fracturing (mode II and III). Each station includes at least 30 fracture orientation measurements (strikes and dips), and measurements of fault planes when existing, using the FieldMove Clino smartphone application of Midland Valley. Validity of these measurements was systematically checked in the field with a compass [Novakova and Pavlis, 2017]. The order of magnitude of aperture, spacing and extension of the main fracture sets was noted (Supp. Mat. 4). The rose diagrams classify fractures into 9 ranges of 20°, centered on zero (N170°–N010°, N010°–N30°, etc...). The convention used is Nxxx° for the strike (NE quadrant), and xx°N for the dip, the last letter giving the dip direction, e.g., N120° 24°E is a ESE plan dipping 24° to the east.

More than 300 stations were analyzed over the entire area. They are grouped when located in the same cell of 4 km^2. In order to characterize fracturing in the infiltration areas that was estimated above an altitude of minimum 2000 ± 300 m from isotopic analyses, [Krimissa, 1995; Taillefer et al., 2018], data measured in high reliefs have been acquired. However, vegetation, quaternary sediments, and access problems explain the irregular density of stations.

The Carança canyon is a deeply incised valley between Thues-les-bains and St-Thomas-Prats-Balaguer hot springs, approximately perpendicular to the Têt fault, that offers the opportunity to realize a scan-line of fractures along a 500 m long outcrop. The fracture orientations have been measured along this profile, 1.5 m above the floor, with a step of ten meters. No corrections (e.g., Terzaghi) have been applied due to the perpendicular orientation of the profile. Secondary faults crosscutting the scan-line have been identified, and fractures have been classified according to the nature of their filling (the different fillings are presented in the results).

3.3 Statistical treatment

Considering the large number of data over a wide area, statistical analysis have been performed in order to reveal correlations between major faults, lineaments, and fractures. Details on the method and all the analyses (PERMANOVA, correlogram and PCA) are given in Supp. Mat. 3. Here is a concise description of each analysis:

PERMANOVA quantifies the dissimilarity between any two objects included in the test, using a pseudo F-test constructed by scalar correlation based on the distance measure. The higher the F-value, the more the hypothesis of statistical differences between groups is true. In our study, PERMANOVA test the potential difference between populations of fractures and lineaments occurring in the vicinity of major faults, considering the respective strike proportions. The p-value obtained by the analyses test the significance of the null hypothesis, i.e. difference between the two dataset.

PCA allows reducing dimensionality of the variable space using a series of new orthogonal variables named "principal components" which records most of the total variability. The principal components provide a large proportion of the total information at contrary of the last component that represents negligible significant. In this work, PCA highlights the potential correlations that typify each population of fracture and lineaments.

Correlogram is a table analyzing the relationship between each couple of numeric variables in a whole dataset. We coupled calculation of the correlation index r with calculation of p-value to remove insignificant correlations from the matrices (p-value > 0.05). In our study, correlogram is mostly used to pinpoint the main correlation between strikes proportions of brittle deformation, in particular to investigate the fracture/lineament relationship.

3.4 Numerical modeling

We use Ibem3D, a 3D angular dislocation numerical model based on linear elasticity (see Maerten et al. [2014] and references therein), to calculate fracture closure (i.e. anticrack normal displacement) and to simulate the reduction of space between contact areas as a

function of compressive confining stress. Fracture geometry is simplified as a single penny-shape 3D dislocation of 1 m diameter, without asperity.

Because the value of current compressive tectonic stress at depth is unclear, we applied a simple condition of compressive-horizontal confining stress due to a lithostatic load ($\sigma_H = \sigma_V.\nu/(1-\nu)$), with a lithostatic stress ($\sigma_V = \rho g z$) corresponding to a range of depth (z) comprised between 500 m and 3000 m, a gravitational acceleration $g = 9.81$ m.s^2, and a rock density $\rho = 2500$ kg/m^3. We performed tests with constant Poisson's ratio $\nu = 0.25$, and variable Young's modulus within a range from $E = 100$ MPa (lower values for metasediments) to $E = 1$ GPa (highest values for gneisses and granites, see Hatheway and Kiersch [1989]).

4 Results

4.1 Lineaments

Lineament mapping is realized in order to reveal geomorphological scars of the surface that are the manifestation of a fault or fracture corridor in surface. The map of lineament density (Figure 3a) reveals that lineaments are highly concentrated in localized spots over the Puigmal range, that nearly corresponds to the infiltration area for hydrothermal fluids (i.e. recharge areas): along the Nuria and Valter faults, and on the Canigou and Cambre d'Aze peaks. Highly concentrated spots also localize around the Llo and Thues hot springs and over the Carança range. Elevated concentrations of lineaments spread more over the Madres range, north of the Têt fault. Low, but not systematically null lineament densities characterize the recent sediments (Neogene basins infills, glacial deposits or alluvions).

Lineaments are analyzed in relation to the strikes of the main brittle faults resulting from the different tectonic stages identified in Section 2: NE–SW (Oligo-Miocene to Plio-Quaternary extension), NW–SE (Plio-Quaternary stage), N–S (unidentified or Plio-Quaternary stage), assuming that lineaments reflect brittle deformations over the Earth surface. Lineament lengths are of the same order of magnitude for the three main directions:

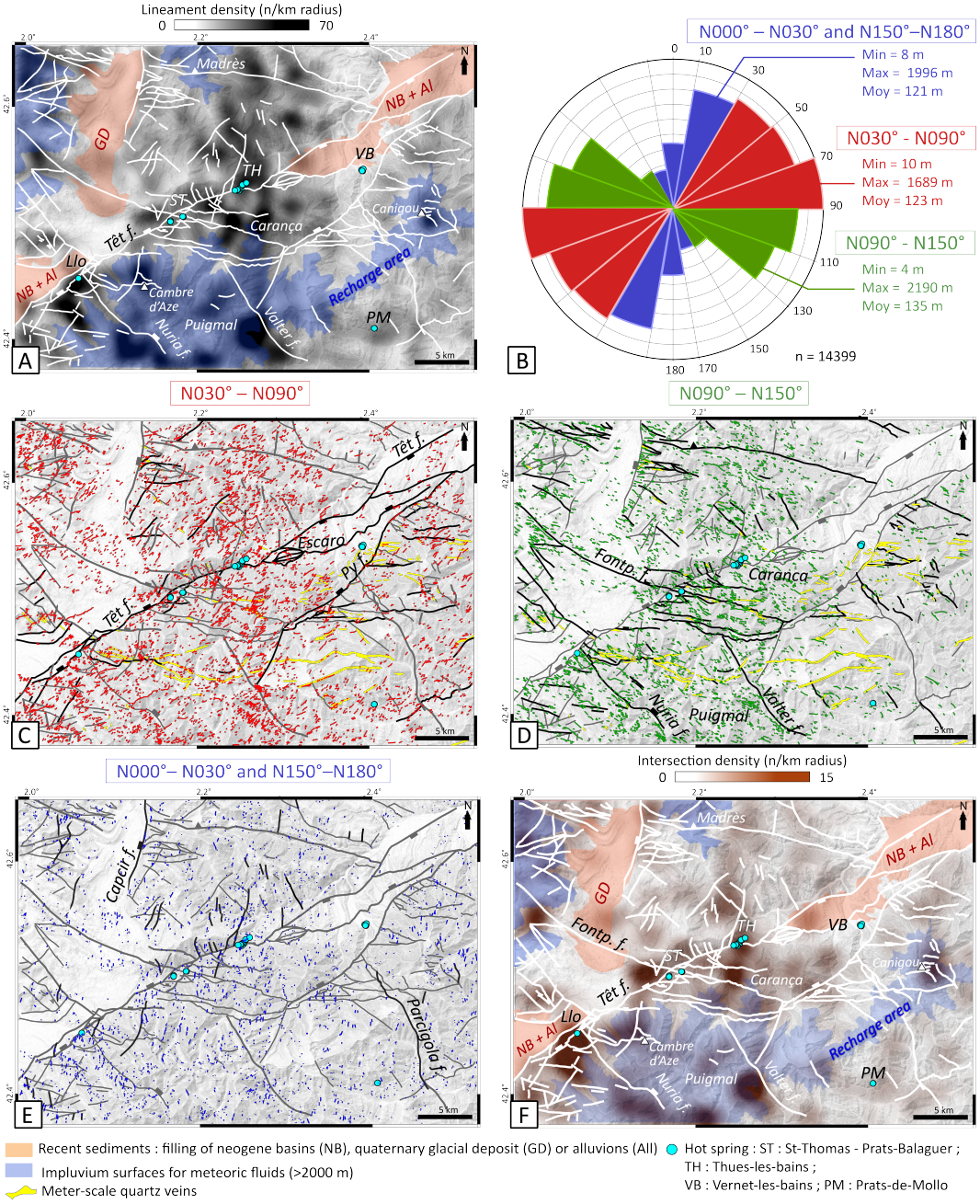

FIGURE 3: Lineament mapping from SPOT 6-7 panchromatic satellite images (1.5 m, Système Pour l'Observation de la Terre), and aerial pictures (5 m) from the IGN=Institut Geographique National (French geographical survey). A) Heat map of lineament density. Recent sediments are mapped: NB=Neogene Basins, GD=Glacial Deposit, All=Alluvions. Recharge areas are located above 2000 m of altitude, B) Rose diagram of total lineaments, C) NE–SW lineaments (N030°–N090°), D) NW–SE lineaments (N090°–N150°), E) N–S lineaments (N000°–N030° and N150°–N180°), F) Heat map of lineament intersections. Data available in Supp. Mat. 2.

minima range between 4 and 10 m, average maxima range from 1689 to 2190 m, and the average size is 124 m (Figure 3b).

The NE–SW lineaments (N030°–N090°, Figure 3c) represent 44.8 % of the total lineaments (n=14399, Figure 3b). N070°–N090° lineaments are relatively the most abundant (16.4 % of the total lineaments). N030°–N050° and N050°–N070° lineaments are present in smaller proportions (respectively 14 % and 14.4 % of the total lineaments). Lineaments occasionally highlight the major faults (e.g., The Py fault, the Escaro relay, or the old Hercynian faults filled by quartz, Figure 3c). NE–SW lineaments can be highly concentrated far from the Têt fault over high-altitude areas such as the Puigmal, Carança and Madres ranges (also see Figures 3a and 4).

NW–SE lineaments (N090°–N150°, Figure 3d) are the second most common (30.1 % of the total lineaments, Figure 3b). N090°–N110° lineaments are the most numerous (13.6 %) in regards to the N110°–N130° (11 % of the total lineaments) and to the N130°–N150° lineaments, the last one being rare (4.8 % of the total lineaments). NW–SE lineaments are highly concentrated on the Caranca and the Puigmal ranges, highlighting or being close to faults with similar strikes (e.g., the Fontpedrouse fault, Figure 3d). They are relatively less common over the eastern part of the study area and over the recent sediment basins. While most of the NW–SE lineaments have N090°–N110° strikes, Figure 3d shows a majority of N130°–N150° lineaments between the similarly oriented Nuria and Valter faults. However, these directions are under-represented among the whole data set (Figure 3b).

The N–S lineaments (N000°–N030° and N150°–N180°, Figure 3e) are relatively rare (25% of the total lineaments, Figure 3b), although N010°–N030° lineaments are relatively abundant (13.4 % of the total lineaments). N150°–N180° and N000°–N010° lineaments are rare (in total, 12 % of the total lineaments). N–S lineaments spread over the entire area without clear relation with the few faults with similar strike (e.g., the Capcir fault). They are highly concentrated around the Llo hot spring.

The map of lineament intersection density (Figure 3f) nearly corresponds to the lineament density map, except near the Madres range where density is high but whereas intersection density is low (Figure 3a). High concentrations of lineament intersections localize over the

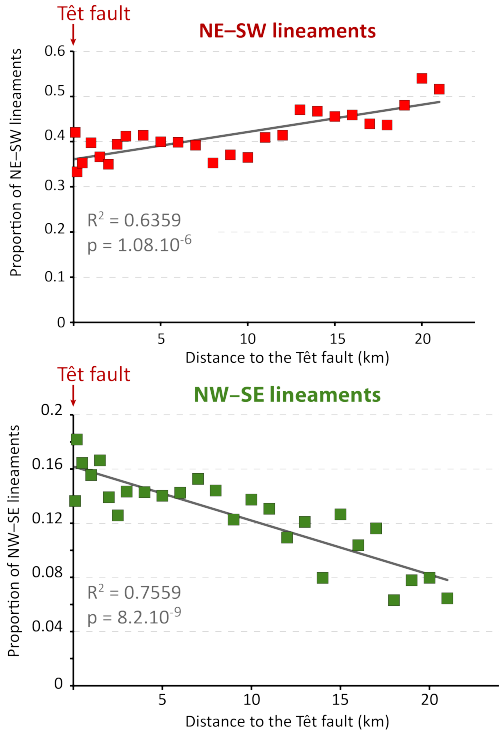

FIGURE 4: Binary diagrams depicting the proportion of lineaments as a function of distance from the Têt fault. The NE-SW lineaments are in red, NW-SE lineaments in green. Symbols correspond to the ratio of strike measurements for a group of lineaments (i.e. NE-SW, NW-SE) as defined in Figure 3, compared to the total amount of lineaments that are comprised within the same range of distance from the Têt fault (e.g., 0-100 m, 100-200 m, etc... see Section 3.1, data available in Supp. Mat.2). R^2 is the correlation coefficient, and p is the statistical significance.

recharge area, in the Puigmal range along the Nuria and Valter faults and the Cambre d'Aze peak, and also over the Carança range. They also localize around the Llo and Thues hot springs, over the Canigou peak, and in two spots along the Fontpedrouse fault, west of the Saint-Thomas hot springs.

A binary plot of the ratio of the different lineament groups compared to the total amount of lineaments comprised in the same range of distance to the Têt fault reveals that the ratio of the NE–SW, and NW–SE lineaments, significantly increases, respectively decreases, with the distance to the Têt fault (Figure 4). Both show good coefficient of correlation ($R^2 = 0.6$ and 0.8, resp.) and are highly significant ($p = 10^{-6}$ and 8.10^{-9}, resp.). The increase of lineament density away of the Têt fault is broadly observed for the N–S lineaments, and not for the fractures (see Supp. Mat. 3).

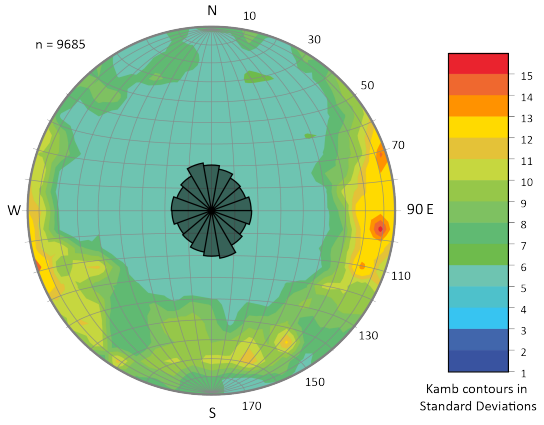

FIGURE 5: Poles contours and rose diagrams (factor two increased) of the measured fractures over the whole study area. Data available in Supp. Mat.4

To summarize, the relative proportions of lineaments in each orientation group reflects the hierarchy of faults in the area. Maximum of lineament strikes corresponds to the large Têt et Py faults, then NW–SE lineaments corresponds to the shorter but numerous NW–SE faults, and finally the N–S lineaments corresponds to the rare N–S faults. Surprisingly, lineaments (strikes and densities) seem not spatially correlated to the main faults. High concentration of lineaments and intersections localize far from the main faults (including the Têt fault) over the highlands in the recharge areas, and around the Llo and Thues hot springs.

4.2 Field data

4.2.1 Fracture data

Fractures data that have been widely measured at a map scale identify which deformation affect rocks far from the main Têt fault, over the recharge areas. Measured fractures in the study area show a wide range of strikes and mainly dip from 70° to 90° (Figure 5). The map distribution of the different strike ranges is described below, in relation to the main fault directions. However, the difference of proportion between each 20° sector does not exceed 2%. From the more to the less evidenced directions:

1. N–S fractures (N000°–N030° and N150°–N180°) are relatively the most common (36 % of the total fractures, Figure 5). The range with the most numerous fractures is N150°–N170° (13% of the total fractures) with sub-vertical dips between 80° and 90°. A main pole of N070° defines a sub-vertical N0160° plan, highly abundant. This range, mainly distributed over the entire area, particularly over the Caranca and Puigmal reliefs, and around the Llo and Prats-De-Mollo hot springs, appears to be relatively rare around the Têt fault (Figure 6, see also Supp. Mat. 3 where fracture strike proportions are interpolated by krigging). The two other N–S ranges (N010°–N030° and N150°–N170°) are rather less common and more spreaded over the entire area. Two main poles of N105° and N110° define two sub-vertical N005° and N010° planes, relatively abundant (Figure 5).
2. NW–SE fractures (N090°–N150°) are relatively the second most abundant (33% of the total fractures, Figure 5). The N090°–N110° range is common along the Têt fault between the hot springs of Thues and Saint-Thomas, including in the hanging wall (Figure 6, also see Supp. Mat. 3). The N110°–N150° range spreads over the entire area. N150° fractures in metasediments north of the Cerdagne basins are the only real major consistent trend over a km-scale distance in the study area.
3. NE–SW fractures (N030°–N090°) are relatively the more rare (30% of the total fractures). A diffuse group of poles define planes between N050° and N120°, that dip between 60° and 80° to the north exclusively, corresponding to the relatively least common classes of fractures, whose minimum ranges between N050° and N070° (10% of the total fractures). This last class is more abundant around the hot springs along the Têt and Py fault, but not over the mountain ranges.

To summarize, the measured fractures at the regional scale present a wide range of strikes without a dominant trend (N–S fractures are the most numerous but with little difference with the less numerous NE–SW fractures), with variable location of density clusters on the map (the N–S fractures concentrate in mountain ranges, and the NW–SE and NE–SW fractures around the Têt and Py faults and the Thues hot springs). NE–SW fractures dip

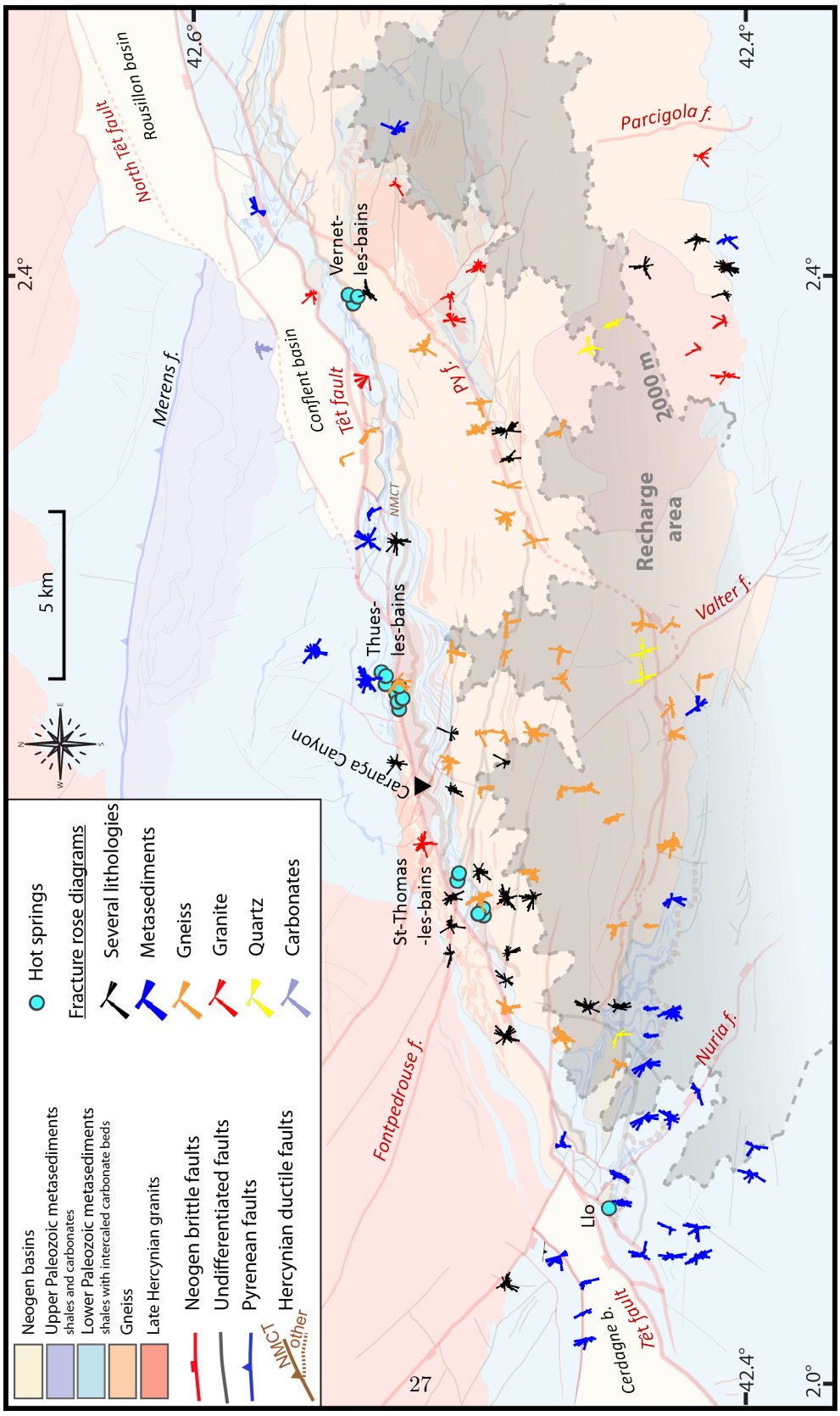

FIGURE 6: Rose diagrams of fractures according to the lithology (structural map modified from Taillefer et al. [2017]). Using the right-hand rule, the petals of the asymmetrical roses include information about the dip direction, that is located on the right of the principal strike. Stations of measurements are clustered when they belong to the same 4 km^2 (see the grid in Supp. Mat. 3). Rose diagram colors correspond to the lithology (when homogeneous). Various lithologies in a same rose diagram are colored in black. Recharge areas (above an altitude of minimum 2000 m $\pm$ 300 m) calculated from the geochemical analyses of Krimissa [1995] and Taillefer et al. [2018] are shaded. Data used are available in Supp. Mat. 4

preferentially between 60° and 80° to the north exclusively.

4.2.2 Faults and fracture outcrops

Fault outcrops provide informations on the CZ compositions, and the organization and filling of fractures in the DZ, that strongly influence the permeability of fault zones and related hydothermal flows. Descriptions of the Têt fault outcrops at Llo and Thues are available in Taillefer et al. [2017]. They show a multi-core fault where cataclastic zones alternate with fractured gneiss lenses, separated by NE–SW but also NW–SE planes.

The Fontpedrouse fault is a NW–SE to WNW–ESE fault that outcrops after the Fontpedrouse village along the RN116 road, in the vicinity of Saint-Thomas hot springs (Figure 7, also see location in Figure 1). This outcrop is located in the Têt fault hanging wall. Vegetation covers the western part of the fault that is likely wider than presented. The Fontpedrouse fault exhibits a single CZ, 10s-m wide. A main N110° 60°N fault plane separates the cataclastic CZ and the fractured granitic DZ (Figure 7a). Whereas the fault plane dips 60°, horizontal striations overprint it, unfortunately without evidence of slip direction.

The CZ is separated into blocks with different degrees of deformation. The fault rocks present typical cataclastic textures according to the Sibson [1977] classification, with fractured, sheared and rotated fragments embedded inside a cataclastic matrix (Figure 7b), crosscut by quartz veins or filled with silicated cement. A major N110° 45°N fault plane with apparent normal displacement and a vertical N150° fault crosscuting it, delimits a central zone of intense deformation composed of silicified cataclasites where even quartz veins are not visible (Figure 7c). This central zone is surrounded by a protocataclastic zone to the east, and a cataclastic breccia zone to the west, where the quartz veins and the rock foliation are still observed.

Many other subordinate faults with various strikes crosscut the fault core. One of them localizes fault breccia and gouges along a N180° 60°W normal fault (Figure 7c). A cleavage is developed inside this fault, and transposed as fractures inside the surrounding fault rocks.

Although crosscutting relationships between faults are difficult to establish, and striation directions are often missing, a chronology of deformation is observable. Observed quartz vein

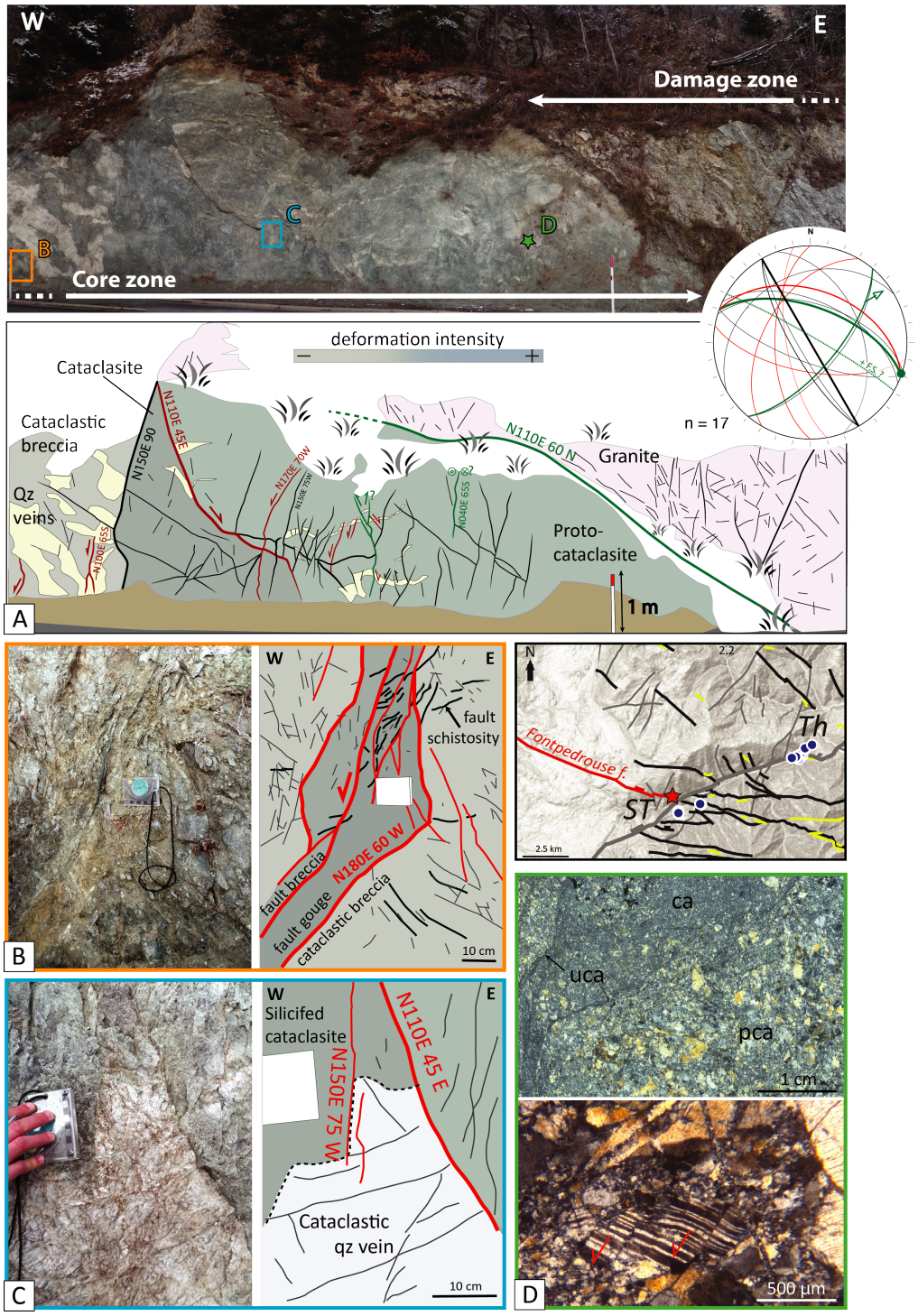

FIGURE 7: The Fontpedrouse fault (N042.50682 ; E002.16748). A) Overview of the cataclastic CZ with the stereographic projections of the fault plans inside it: green: strike-slip evidence, red: normal slip evidence, F.S.: flower structure, B) Cataclastic texture inside the CZ (sheared and rotated fragment inside the cataclastic matrix - the two pictures are different views in the same thin-section) ca: cataclasite, pca: protocataclasite, uca: ultracataclasite, C) fault planes inside the CZ delimiting the deformation zones. D) Fault gouges and breccias inside the CZ.

displacements are consistent with normal kinematics of the N110° faults. Several N040° and N150° to N180° steeply dipping faults (80-90°) with apparent normal displacements, seem to cut all the other faults, including the fault plane that separates the cataclastic zone from the cataclastic breccia zone (Figures 7a, b and c). The only fault striation with an observable shear sense reveals a likely left-lateral strike-slip, along a N040° 65°S fault (Figure 7a). A N120° subvertical fault looks like a positive flower structure. Finally, low dipping faults (30°) with various strikes (e.g., N060°, N160°, N120°) are also crosscuted by the high dipping faults.

The Carança canyon, located in the Têt fault footwall (location in Figure 5) cuts across the NMCT at is entrance, then mainly the Carança gneissic dome, and occasionally thin quartz or carbonate levels and pegmatite dykes. The canyon is intersected by faults and fractures (Figures 3 and 8a). The NE–SW faults are rare, they show dip-slip without evidence of sense of shear. The numerous sub-vertical N110°–N130° faults are strike-slip, mostly dextral, but striations overprint more dipping striations, likely normal because of the sub-vertical dip. Most of these faults have brittle attributes (striations, cataclastic rocks) except one of them that localizes cataclastic breccia inside a pre-existing ductile foliation (Figure 8b). Finally, N170°–N180° sub-vertical faults have subhorizontal sinistral striations.

Different fractures, according to their filling, are differentiated along the scan-line (Figure 8c):

1. Subhedral quartz veins filled by cm-scale quartz crystals, covering open walls. The main orientation of these veins is subvertical N030°, some of them are N090° dipping 60° to the north exclusively.
2. Anhedral quartz as silicate coating with quartz crystals invisible to the naked eye, smaller than the millimeter size. These plans are mainly oriented N110°, dipping between 80° and 60, few of them are subvertical N030°.
3. Numerous calcite filling as powdered white plating. Their composition has been validated with X-ray diffraction [Taillefer et al., 2017]. The strikes are scattering, subvertical and oriented between N030° and N150°. Some N070° to N090° fractures dip

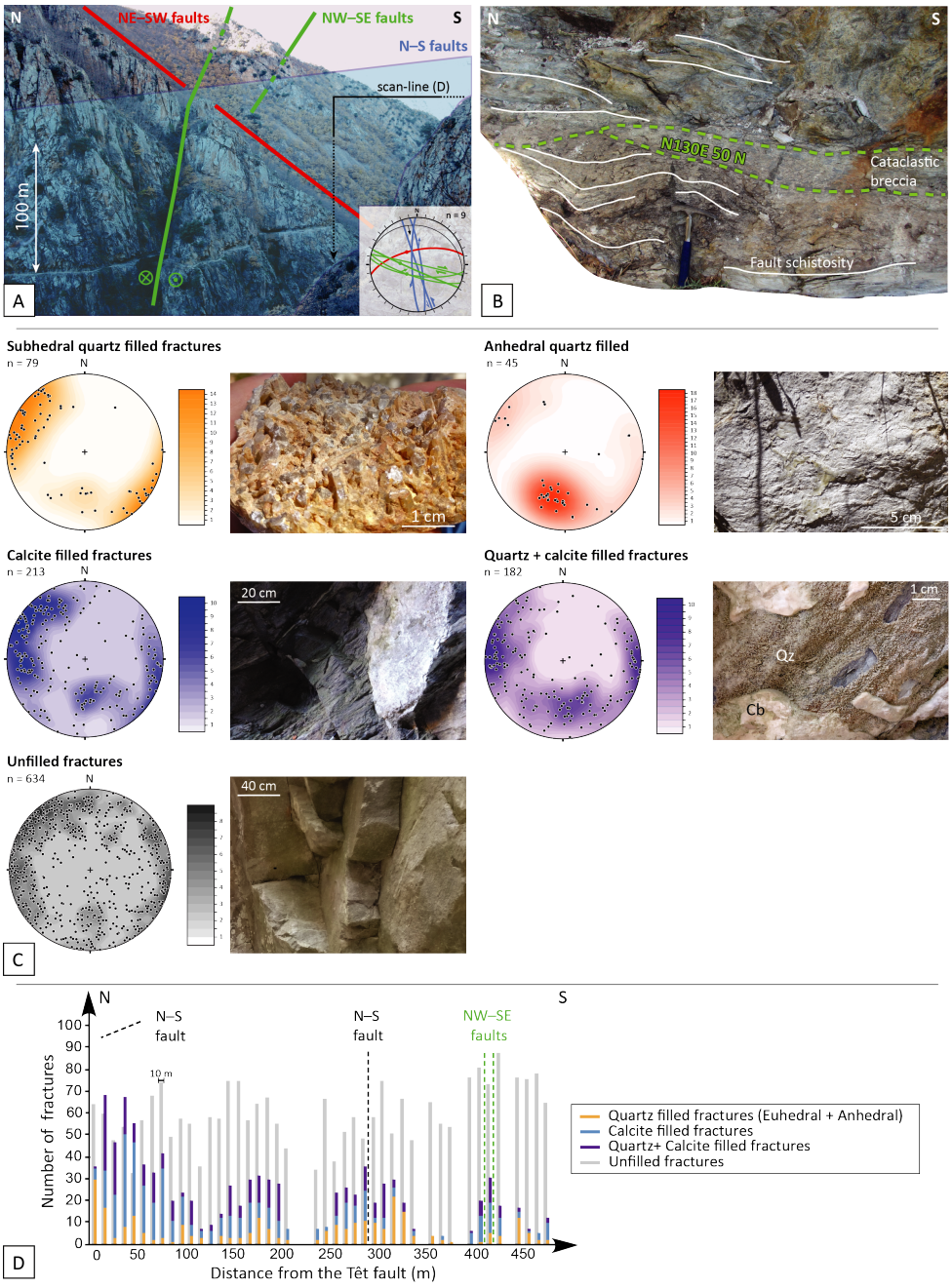

FIGURE 8: Faults and fractures inside the Carança canyon (see location Figure 6). A) Landscape view of the Carança canyon, and stereograms of the faults. View since N042.51470 ;E002.22482, B) Outcrop of a NW–SE ductile fault reactivated as brittle (N042.51799 ;022.22368, C) Stereograms and pictures of the different types of fracture filling, D) Scan-line of fractures amount each 10 m as a function of the filling. The scan-line starts at the Têt fault, in the footwall, at the entrance of the canyon (N042.52166 ;E002.22173). No corrections (e.g., Terzaghi) have been applied.

60° to the north.

4. Combination quartz + calcite: subhedral quartz coated by calcite. These fracture strikes are scattering and have two main concentrations: N–S subvertical fractures, and N060°E to N100°E fractures dipping 80° to 60° to the north.
5. Unfilled fractures are the most numerous fractures. They have scattered distribution, mainly subvertical, with a small concentration of N090° fractures dipping 80° to 60° to the north.

The amount of all the mineralized fractures generally decreases with distance to the Têt fault (Figure 8d). The number of mineral-filled fractures locally increases in the vicinity of secondary faults, whereas unfilled fractures follow a more constant distribution.

In brief, polymodal orientations observed at the map scale are also observed in the field. This deformation is mostly brittle (cataclastic rocks, striation, fracturing), and may be superimposed on earlier ductile deformation (N130° faults). N–S faults show evidence of sinistral slip on sub-vertical faults, or superimposed on normal faults, crosscutting the other faults. Most of the subhedral quartz veins correspond to this orientations (N030°). NE–SW faults have moderate dip (60-70°) mainly to the north, that show normal dip striations [Taillefer et al., 2017]. N090° to N130° faults, as the Fontpedrouse fault, are major brittle faults dipping subvertically or around 60°, with apparent normal displacement, and mainly dextral superimposed strike-slip striations. Anhedral quartz veins correspond to these orientations, which is not systematic for subhedral quartz veins.

4.2.3 Fracture vs lithology

Variations of fracturing according to the lithology are investigated in order to understand if these could explain the exclusive location of hot springs in crystalline rocks in the vicinity of a contact with metasediments. The lithology distribution over the study area is not homogeneous (Figure 6). Gneiss composes most of the Têt fault footwall, all along the center and the eastern part of the study area. Metasediments occupy the eastern part of the Têt footwall, all the south of the Têt fault, and some patches over the Canigou range

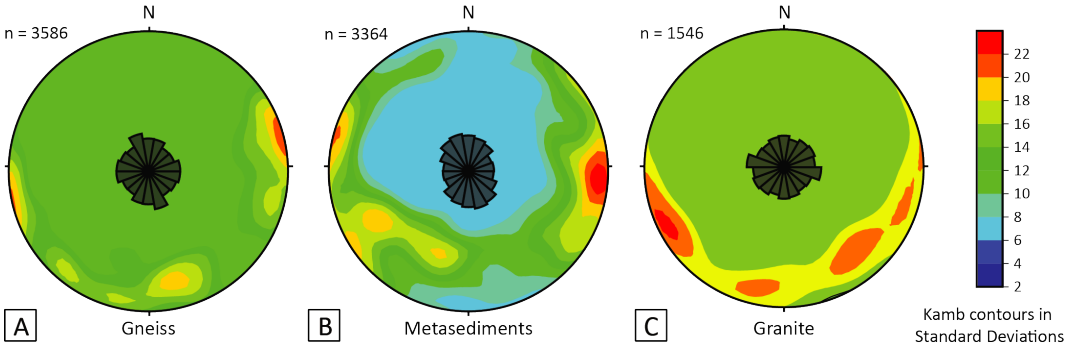

FIGURE 9: Rose diagrams of fractures according to lithology: A) in gneiss, B) in metasediments, and C) in granites. Data are available in Supp. Mat.4

and along the central part of the Têt fault. Granites occupy the western part of the study area, and some patches inside the Py fault footwall. Numerous measurement stations overlap multiple lithology.

Stereograms of fractures according to lithology (Figure 9) look similar to the general fracture stereogram (Figure 5) with subvertical fractures and scattered orientations. For the gneiss and metasediments (Figure 9a and b), most of the fractures are N–S, consistently to the general stereogram. In gneiss, the greater proportions of fractures are oriented N150°–N170°, with subordinate clusters is also observed between N000°–N030° and between N070° and N110°, and a minor proportions for the N030°–N070° and the N130°–N150°. In metasediments, most of the fracture strikes are scattered between N000° and N050° and between N150°–N180°, with less numerous fractures between N050° and N130°. Fractures in granites (Figure 9c) are less numerous than in gneiss or metasediments, that could explain why their different strike are not prominent in the general fracture stereogram (Figure 5). Despite a wide spread in fracture strikes, the N090°–N110° appears to be abundant. Finally, all the lithologies record south poles of NE–SW to NW–SE fractures with dip about 60-80° to the north, which are particularly well developed in metasediments.

For each outcrop, our data include the order of magnitude of aperture and spacing for each fracture main direction. The general fracture aperture observed in metasediments is usually smaller than in crystalline rocks (Figures 10a and b, respectively). Fracture apertures

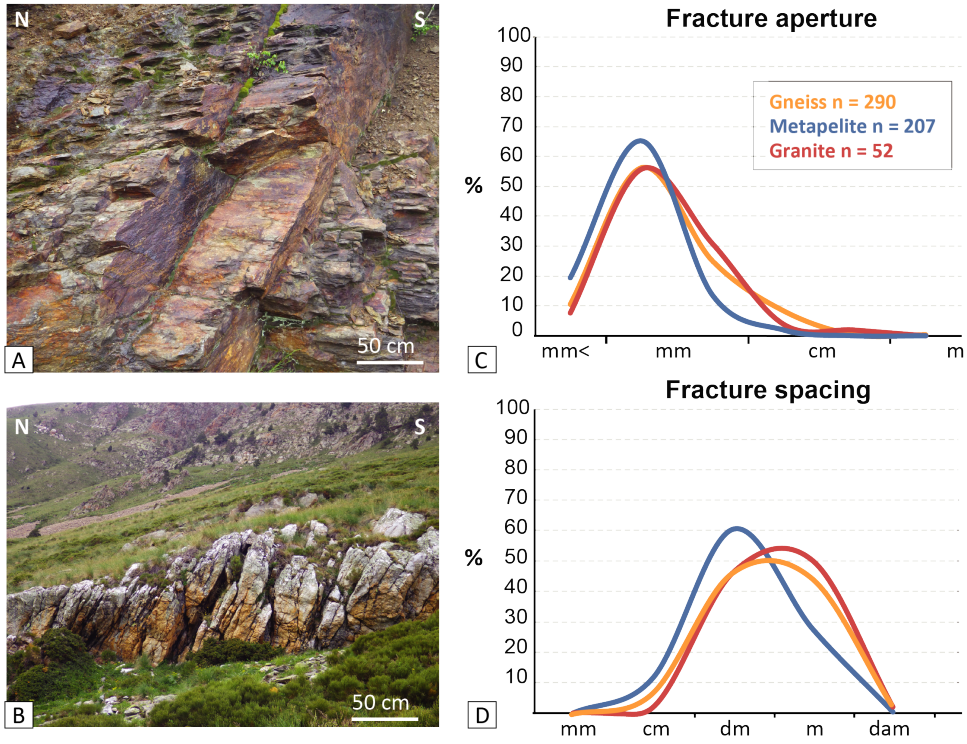

FIGURE 10: Fracture features in the field. A) Closed fractures in metasediments. B) Opened fractures in crystalline rocks. C) Distribution of fracture aperture according to the lithology. D) Distribution of fracture spacing according to the lithology. Data available in Supp. Mat.4

and spacing follow an unimodal distribution (Figure 10c and d, respectively), with gneiss and granite following the similar trends. Fracture aperture mode is centered on millimeter scale openings (Figure 10c). However, fractures with apertures larger than the millimeter size are more numerous in crystalline rocks than in metasediments, while apertures smaller than the millimeter are more frequent in metasediments.

Fracture spacing for metasediments range from m to dm and the mode is centered on dm (Figure 10d). The crystalline rock curve spreads more broadly, from 10s-cm to m.

4.3 Fracture closure numerical modeling

Fault and fracture observations presented in the previous section only deal with data acquired at the surface. Many works focus on experimental analysis on samples to estimate permeability and stiffness of fractures under confining stress, as expected at depth (e.g., Pyrak-Nolte and Morris [2000]). Another complementary way to estimate fracture aperture as a function of depth is to perform numerical modeling of pressure-induced fracture closure.

In accordance with the models, Figure 11a is based on displacement of the fracture sides, i.e. the fracture closure. Confining pressure must increase fracture closure with depth if stresses responsible for fracturing (such as fluid pressure) are relaxed and the fractures are incompletely filled (Figure 11b). For the Young's modulus used in the model and for the considered fracture, the fracture closure computed for 3000 m depth is one order of magnitude larger than the closure computed for 500 m depth, i.e. 5 mm at 500 m and 1 cm at 3000 m for the lowest Young's modulus ($E = 10^9$, metasediments). The higher the Young's modulus (gneiss, granite), the smaller the closure, i.e. between 0.1 mm and 5 mm for gneiss and granites and between 1 cm and 1 dm for metasediments.

In order to discuss fracture aperture at depth for our study case, we applied the different trend of closures vs. depth laws from Figure 11b to the average of fracture apertures observed at the surface (i.e. gneiss and granite: 3.7 mm ; metasediments: 2.5 mm, Figure 10c, see Supp. Mat. 4). End member values of Young's modulus for each lithology (4.10^4 to 10^5 MPa for gneisses ; 10^4 to 9.10^4 MPa for granites ; 10^3 to 6.10^4 MPa for metasediments ; see Hatheway and Kiersch [1989]) are considered to estimate a range of possible apertures at depth (Figure 11c). As shown in Figure 10c, gneisses and granites have a similar behavior, thus we define only one type for both, termed as crystalline rocks.

Fracture aperture at a given depth, and for a given surface fracture aperture, is lower in metasediments than in crystalline rocks (Figure 10a, b and c and 11c). Even at shallow conditions (500 m depth), fracture apertures in metasediments appear much lower than in crystalline rocks, partly because of their smaller aperture at the surface, and mostly because of the low Young's modulus of metasediments. The lowest Young's modulus used

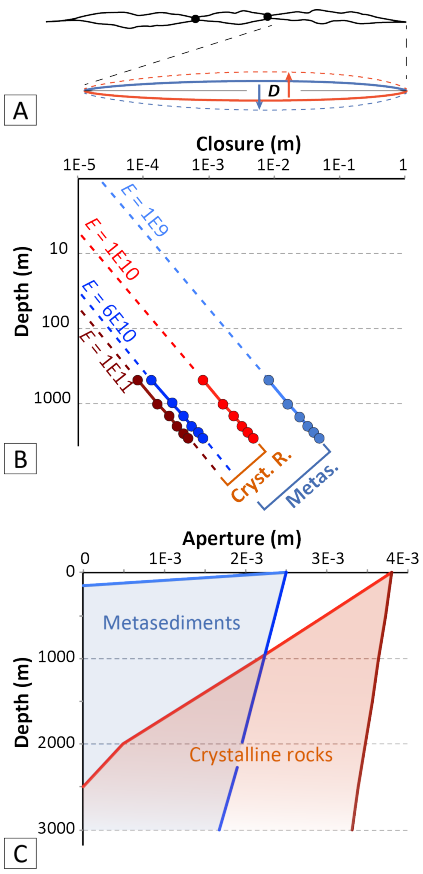

FIGURE 11: Dislocation numerical models. A) The model considers a 1m-long simplified closed fracture, which, by allowing inter-penetrative movements, corresponds to the closure (D=displacement) of an opened fracture, B) Evolution of fracture closure with depth according to the ranges of Young's modulus (E) for crystalline rocks and for metasediments (log-log scale), C) Application of the closures calculated by the model (B) to the observed fracture aperture at the surface (Figure 10c).

for crystalline rocks ($E = 10^6$ MPa) does not allow a complete closure of the fractures before 2500 m of depth, while the highest values still predict open fractures at 3000 m depth.

5 Discussion

5.1 Fault and fracture distribution, opening, and their origin

5.1.1 Deformation scaling evidenced by statistical analysis

In order to unravel the complex relationship between the main faults, secondary faults, and fractures, we performed statistical treatment of the datasets (Supp. Mat. 3). Statistical analysis reveals that the strike proportions of lineaments and fractures are not spatially correlated. It also reveals that the Têt fault does not regionally influence fracture strikes and has a larger influence on lineament strikes, i.e. secondary faults or fracture corridors, at a regional scale than at the 100s-m scale (Figure 4). The three scales of brittle deformation, i.e. kilometric faults, secondary faults, fractures, accommodate with different strikes the regional stress-field. This phenomenon has recently been evidenced in basement rocks by Luby et al. [2020] using multi-scale remote sensing in western Egypt. Consistently, applications of recently developed statistical analysis have revealed that fracture patterns may be clustered, randomly spaced or evenly spaced [Marrett et al., 2018; Wang et al., 2019]. The reasons for this paradox are discussed below.

5.1.2 Background fracturing

Variations of fracture strikes with distance from a lineament (i.e. secondary fault or fracture corridor) before reaching the "background fracturing" have been also reported by Gabrielsen and Braathen [2014]. Shallow fractures constituting the background fracturing likely originate from various processes, that have affected the study area, including tectonic stresses, fluid pressure, crust exhumation, topographic stresses [Banks et al., 1996; Clarke and Burbank, 2011; Earnest and Boutt, 2014; Leith et al., 2014a], and potentially also cycles of glaciation/deglaciation [Carlsson and Olsson, 1982; Augustinus, 1995; Jarman et al., 2014; Leith et al., 2014b].

Along the scan-line (Figure 8), unfilled fractures show any spatial trend with respect to

the Têt fault distance, but similar strikes than the total fractures in the entire area (Figure 5). This seems to confirm that unfilled fractures mainly correspond to background fracturing formed at shallow depths [Peacock et al., 2016], and that they are likely marginally related to faults.

5.1.3 N–S fractures as part of the background fracturing

The abundant proportion of N–S fractures (Figure 5) represents an important part of the background fracturing in the study area. Low amount of N–S major and secondary normal faults suggests that N-S faulting is not the main process controlling the formation of N-S fractures (Figure 3e). N–S fractures have been described north of Conflent by Arthaud and Pistre [1993] and are commonly attributed to the N–S Pyrenean compression [Arthaud and Mattauer, 1969, 1972; Ballas et al., 2012; Tavani et al., 2020]. Where N-S fractures clusters are observed (e.g. at the Llo hot spring, see Taillefer et al. [2017] and Supp. Mat. 3) it could not be excluded that a part of these fractures have formed during the strike-slip reactivation of the Têt fault. These N–S fractures could have been reactivated as seen on N–S brittle faults (Figures 7 and 8) during latter tectonic stages favorable to N-S faulting, as observed in Neogene sediments by Baize et al. [2002] and Delcaillau et al. [2004].

5.1.4 The concentrated deformation related to the Têt fault

Poor correlations between major and secondary faults highlight two levels of deformation distribution: concentrated around the major fault zones (CZ+DZ), or regionally distributed away from the major faults over the adjacent highlands in the form of secondary faults (i.e. lineaments, Figure 3). There are several points as possible explanations for the spatial distribution of both the NE–SW and NW–SE lineaments with respect to the Têt fault (Figure 4).

At the Têt fault zone, the master fault orientation is likely able to accommodate regional stress and deformation may concentrate inside the pre-existing fault core rather than creating new structures (i.e. NE–SW secondary faults). This is supported by the limitation of DZ growth within a few hundred of meters for fault displacement larger than 300 m

[Savage and Brodsky, 2011], which is potentially controlled by the crust thickness [Mayolle et al., 2019]. Due to this Têt fault reactivation, in its vicinity, the regional stress-field can be partially relaxed and modified, preventing the formation of NE–SW secondary faults (e.g. Ackermann and Schlische [1997], and Gupta and Scholz [2000]), favoring faulting with different orientations [Kattenhorn and Pollard, 2001; Faulkner et al., 2006; Gabrielsen and Braathen, 2014; Marrett et al., 2018].

5.1.5 The distributed NW-SE faults

Because it is now obvious that NW-SE faults have formed during successive deformation stage (Figures 7 and 8b), their timing during the Cenozoic period is not easy to establish. This study provides new arguments to clarify and constrain this deformation:

Firstly, N100° to N130° faults have brittle features (Figures 7 and 8), meaning that they were active when the crust was at shallow structural levels. i.e. after the Pyrenean compression. Indeed, the Aspres and Canigou nappes have constituted at least 5 to 10 km of rock thickness above the study area [Ternois et al., 2019]. The ductile feature of the NW-SE brittle faults (Figures 7 and 8b) could be inherited from the Pyrenean period or be a reactivation of ductile Hercynian deformations [Guitard et al., 1992, 1998; Autran et al., 2005; Laumonier et al., 2015a,b, 2017].

NW–SE major brittle faults are often abutting against the NE–SW faults (e.g., the Têt and Tech faults, see Figures1 and 3) or intersecting them (e.g., the Valter and Py faults). These two criteria suggest that the NW-SE faults post-date the formation of the NE-SW faults, i.e. the main Oligo-Miocene extensional stage [Aydin, 2000; De Joussineau et al., 2005; Mynatt et al., 2009]. If the orientation of the stress field had changed after the Oligo-Miocene, e.g. in a NE-SW extension, the Têt fault could have been reactivated and allowed extensive quadrant normal faults due to oblique dextral strike-slip (e.g. Chester and Logan [1986], Kim et al. [2001], and Ishii [2016]). This would result in NW-SE fault orientations in its vicinity, explaining the high concentration of NE-SW lineaments in the Têt fault vicinity (Figures 3 and 4).

In addition, new thermochronological data provided in the area by Milesi [2020] reveal

differential exhumation along the Têt fault between 18 and 10 Ma. During this period, the NW-SE faults were activated with vertical motion, probably with normal kinematics (fault dip is large), and then much earlier than the NW-SE faulting observed in Cerdagne by Cabrera et al. [1988] and Delcaillau et al. [2004].

According to the kinematic evidence along NW–SE brittle faults in French Eastern Pyrénées and Catalonia (Figure 2) and in agreement with Cabrera et al. [1988] and Mauffret et al. [2001], we propose that the brittle activity of these faults may start as partitioning strike-slip faults during the Oligo-Miocene extension, and as normal fault during an later extensional stage, likely of middle-Miocene to Pliocene (Figure 12). This last extension would have preceded the NE–SW extension in Catalonia (Figures 1 and 2), revealing a migration of the deformation from North to South. Reactivations of the NW-SE Hercynian ductile fault of Merens (NW of the study area, see Figure 1) have also been evidenced as reverse during the Pyrenean compression [McCaig and Miller, 1986] and as normal and strike-slip during the Quaternary [Gourinard, 1971; Turu and Planas, 2005].

This extensional stage is not only accommodated by displacements along km-scale faults, whose large CZ thickness results from the addition of previous strike-slip and normal motions (Figures 7 and 8), but also by secondary faults (i.e. lineaments, Figures 3 and 4). The Neogene deformation appears distributed over the study area in the form of some major normal faults, and many secondary ones (NE–SW and NW–SE, see Figure 3). These distributed deformation may contribute to the continuous crustal thinning observed by Chevrot et al. [2018] and Diaz et al. [2018] (Figure 1, see Section 5.4). This distribution would explain why the major NW-SE faults are not marked by important scarps in the landforms. Moreover, scarps formed during the middle Miocene as suggested, we prone to be significantly eroded during the upper Miocene (Messinian) and Plio-quaternary periods. This contrasts with the well preserved NW-SE scarps in Cerdagne, still active much later [Cabrera et al., 1988].

Finally, also note that evidence of super-imposed strike-slip or reverse slickensides on NW-SE 60°N dipping faults (Figure 7) indicate a subsequent N–S compressive event, in agreement with many observations in the French Eastern Pyrénées and the recent stress field (Figure 2, Cointre [1987], Philip et al. [1992], Calvet [1999], Goula et al. [1999], Delcaillau

et al. [2004], Chevrot et al. [2011], Rigo et al. [2015]).

5.1.6 Mineralized fractures

At the 100s-m scale, mineralized fracture density (i.e. veins) decreases with the distance to the Têt fault, as usually observed in fault DZ (Figure 8, Anders and Wiltschko [1994], Forster et al. [1997], Mitchell and Faulkner [2009] and Savage and Brodsky [2011]). Consequently, subhedral quartz veins should have formed at depth during the Têt fault activity, and have been then exhumed [Peacock et al., 2016]. NW–SE anhedral quartz-filled fractures are likely subhedral quartz veins that have been reactived (and then crushed) because of a favorable stress field (consistent with a Mio-Pliocene extension stage).

Calcite-filled fracture strikes are more scattered than quartz-filled fractures, and post-date the subhedral quartz, suggesting that carbonate-rich fluids used the existing fracture network, veins and shallow joints [Stober and Bucher, 2015]. However, their high concentration in the Têt fault (Figure 8c) suggests that they have circulated during a recent (shallow) reactivation of the fault. As silica + carbonate sinter or fracture filling are common in the vicinity of active hot springs [Campbell et al., 2002; Smith et al., 2011] and/or fault DZ associated with hydrothermal systems [Bruhn et al., 1994; Caine et al., 2010; Taillefer et al., 2017], the carbonate-rich fluid could also be linked to a past fluid circulation related to the modern geothermal system. Accordingly, sealing of the fracture network by late carbonate precipitation could explain the absence of hot spring at the Carança valley entrance, although a thermal anomaly is observed in the numerical model of Taillefer et al. [2018]. This would imply that the permeability network has not been sealed around the other hot spring sites, because of recent deformation, and seismicity [Lowell et al., 1993; Banks et al., 1996; Renard et al., 2000; Cox et al., 2015; Belgrano et al., 2016].).

5.2 Impacts on fluid flow

5.2.1 Fault and fracture intersections

The fault and fracture networks are distributed over the entire area, with various strikes, that locally result in clusters of intersections (Figures 3d, 6 and 8c). On the vegetation cover map in Supp. Mat. 2, high lineament density that appears in dense forest areas in the vicinity of major faults (as well as in highlands), indicate that the interpretation bias related to the vegetation is limited. It cannot be excluded that the lineament density map (Figures 3a and d) underestimate secondary fault density, especially in areas of thick vegetation cover and soil, because high fracture density enhances erodibility and weathering (e.g. Steer et al. [2011], Hasenmueller et al. [2017]). This is the case at the area of St Thomas hot springs, were the rocks are particularly damaged due to pronounced fault intersections, and where the soil is particularly well developed.

The clusters of lineament intersections indicate that meteoric fluid infiltrations are favored over the recharge areas (i.e. above an altitude of minimum 2000 m ± 300 m, Taillefer et al. [2018]), mainly along NW–SE faults, i.e. the Nuria, Valter, and Fontpedrouse faults. These faults crosscut the Têt fault, concentrate secondary fault intersections in their vicinity, and provide migratory pathways from the high infiltration zones into the Têt fault hydrothermal system. Thues and Llo hot springs also correspond to high intersection patches, suggesting efficient discharge points, as documented in other settings [Curewitz and Karson, 1997; Person et al., 2012; Belgrano et al., 2016]). The Vernet hot springs are not related to high lineament intersections, but actually correspond with areas covered by recent sediment deposits that may constitute a detection bias. Saint-Thomas is actually located at the intersection between the Têt fault with the NW–SE Prats fault that likely drives meteoric fluids directly to the Têt valley, under the influence of topographic gradient [Taillefer et al., 2018]. It is highly probable that high lineament density exists in St Thomas, as suggested by the pronounced intersection of NW–SE faults. This is actually less obvious for Vernet since fluid flow is thought to be rather controlled by a combination of both ductile fault juxta-

position (NMCT) of metasediments above gneisses and local topographic effects (Taillefer et al. [2017], see below).

In agreement with the polyphased history, we propose that some of the NW–SE faults are reactivations of shear zones, old faults, or lithological contacts, that have favored hydrothermal fluid flows in their DZ [Mazurek, 2000; Bertrand, 2016; Belgrano et al., 2016; Taillefer et al., 2018]. The fine cataclasites inside the NW–SE fault CZ (Figure 7), likely poorly permeable, could compartmentalize different fluid reservoirs inside the basement, as proposed in Conflent by Arthaud and Pistre [1993].

5.2.2 Lithological controls

These high permeability zones observed at the surface extend at depth, helped by the abundance of favorable lithologies (i.e. crystalline rocks) below the recharge areas (Figure 6). Gneisses and granites, whose fracture apertures are higher at the surface, and likely at depth, than in metasediments (Figures 10 and 11), cover 70% of the recharge areas. In agreement with our model, open fractures and hydrothermal alterations have been observed in crystalline rocks at a depth of 3600 m at Soultz-sous-Forêt [Benderitter and Elsass, 1996], where granite could even be more permeable than gneiss, favoring fluid channeling [Stober and Bucher, 1999]. Crystalline rocks is a general requirement of topographic hydrothermal systems according to thermal modeling [Wanner et al., 2020].

Differences between metasediment and crystalline rock permeability is a direct function of fracture length and aperture distributions, and the resulting connectivity (see Barton et al. [1995]). These differences in fracture aperture between lithologies are observed at the microscopic scale by Bertrand [2016]. Although the simple dislocation model performed in this study does not consider a large variety of factors able to influence permeability (i.e. aperture irregularities, roughness and dip, fracture network connectivity and complexity, sealing by fluids deposits, alteration, and seismic activity), the results agree with numerous studies about permeability decrease with depth (e.g. Snow [1968], Ingebritsen and Manning [1999], Saar and Manga [2004], and Ingebritsen and Manning [2010]). Ranjram et al. [2015] observe that the lithology may be an important control of permeability decrease with depth,

and that crystalline rocks may have a high permeability at depth, but also recognize that the complexity of a fractured media does not allow easy prediction of a law for permeability decrease.

Following Earnest and Boutt [2014], we propose that, in the study area, fluid infiltration, downward and upward flow is favored by the presence of crystalline rocks rather than metasediments. This explains the exclusive location of the Têt hot springs in crystalline rocks, and in particular close to fault juxtaposition contacts with impermeable metasediments [Taillefer et al., 2017]. It is interesting to note that all the other hot springs in Eastern Pyrénées that are not related to the Têt fault are actually located at this interface (e.g. Ax-les-thermes, Merens-entre-Valls, Amélie-les-bains, Prats-de-Mollo-La-Preste, Molitg-les-bains, etc... see Figure 1). In addition, the collocation of deep epicenter (10-20 km) and the warmest hot springs (Thues, St Thomas) suggests that the current seismic activity could allow hydrothermal flows up to 10 km of depth, as demonstrated by Diamond et al. [2018] and Wanner et al. [2020].

Summarizing previous studies of orogenic-belt related hydrothermal systems, favorable areas for geothermal exploration, including where fluids emergences do not reach the surface (e.g., buried below sediments), could be determined by mapping a combination of: a) bottom of valleys bordering mountain ranges where the topographic gradient is the highest [López and Smith, 1995; Taillefer et al., 2017; Wanner et al., 2020], b) high lineament density suggesting important fluid pathways (recharge and upflow, e.g., this study), c) DZ of active or recently-activated faults, especially at fault intersections [Curewitz and Karson, 1997; Schneeberger et al., 2018; Taillefer et al., 2018], d) crystalline massif bordered by metasediments (Taillefer et al. [2017] and this study), and d) mineralized or travertine areas [Caine et al., 2010; Belgrano et al., 2016].

5.3 Model of faulting, fracturing, and establishment of the Têt hydrothermal system

Combining previous works with our new field data and lineament mapping, numerical models and statistical analysis, we propose a new model linking the evolution of faults, fractures and their associated permeability with the establishment of the Têt hydrothermal system (Figure 12):

NW–SE ductile faults inherited from the late Hercynian period may be reactived firsts during Pyrenean compression, as evidenced by the Merens fault north of the study area (McCaig and Miller [1986], Figure 12a). Numerous N–S mode-I fractures form throughout the upper crust. Although relief exists, metasediments cover the Canigou crystalline dome, preventing the establishment of shallow hydrothermal circulation (Figure 11).

Then, Oligo-Miocene extension induces the formation of the Têt and the Py normal faults, with DZ providing highly permeable zones, especially at fault relays (Curewitz and Karson [1997]; Person et al. [2012], Figure 12b). Displacement localizes along the Têt fault zone preventing a large expansion of the DZ [Faulkner et al., 2006; Savage and Brodsky, 2011]. Away from this zone, the deformation is distributed as numerous secondary NE–SW faults extending up to the surrounding high altitudes. Intersections of these faults with previously formed N–S fractures, freshly exhumed and re-opened, provide a high permeability network for meteoric fluid infiltration (i.e. recharge areas, Schneeberger et al. [2018]). The progressive exhumation of the Têt fault footwall increases the pressure gradient for driving convection [Taillefer et al., 2018] and the exhumation of the Canigou-Carança crystalline dome, where fracture apertures could remain open at depth (Figure 11). Due to the unroofing of the meta-sediments, it is likely that the onset of hydrothermal circulation was established during this period.

Later, the Middle-Miocene to Pliocene NE–SW extensional stage (Figure 12c) allows the development of NW–SE brittle faults (some of them reactivate Hercynian faults), similar to deformation in Catalonia (Tranverse ranges, El Emporda, Figure 2) but likely earlier.

Because of the previous Têt fault activity or its oblique reactivation [Delcaillau et al., 2004], NW–SE secondary faults or fracture corridors rather concentrate in its vicinity providing new efficient discharge pathways. Numerous NW–SE major and secondary faults also intersect the adjacent reliefs, providing 1) numerous intersections with the previous N–S fractures, NE–SW secondary faults, and with the background fracturing that continue to be exhumed (i.e. re-opened) together with the Canigou crystalline dome, and 2) major brittle DZ that connect fluid pathways from elevated relief to the Têt valley [Taillefer et al., 2018]. Given that the current topography has been already acquired, it is likely that the hydrothermal system is already established. Its subsequent evolution is a function of the sealing-opening cycle of the fracture network.

Last, the Plio-Quaternary period is characterized by a return to a compressive regime in the Eastern Pyrénées (Figure 2). NE–SW and NW–SE faults could have been reactivated as strike-slip or even as reverse slip during the Plio-Quaternary (Figures 7 and 8, Cointre [1987], Guitard et al. [1998], Calvet [1999] and Goula et al. [1999]). However, field observations do not allow a precise direction to be defined for the recent or current compressive stress, which is probably N–S $\pm$ 20° [Rigo et al., 2015]. N–S normal faults (e.g. the Capcir and Parcigola faults) are necessarily post-middle-Miocene, because the basin filling of the Capcir fault likely corresponds to the Cerdagne basin filling, and postdate all the other deformations (Figure 7a). However, the timing of their formation remains difficult to establish, and specific studies are required. In addition, evidence of normal faulting in Roussillon terraces [Delcaillau et al., 2004; Carozza and Baize, 2004] and in Cerdagne middle-Miocene sediments [Baize et al., 2002] demonstrate the variability of the stress tensor [Goula et al., 1999; Rigo et al., 2015]. This transient stress field maintains open most of the previous faults and fractures, and sustains the activity of the hydrothermal system. Meteoric water is then preferentially infiltrated in crystalline rocks widely cropping out in the recharge areas. Additionally, glaciation cycles and topographic evolution likely continue to create or maintain open shallow fractures [Jarman et al., 2014; Delmas et al., 2018]. At depth, the water may flow into the volume of crystalline rocks corresponding to the Canigou-Carança ranges, as well as below the Paleozoic metasediments of the Puigmal Range.

5.4 Geodynamic implications

Investigations of the Pyrenean crust thickness show a lack of a crustal root in the Eastern Pyrénées, with a progressive Moho shallowing from West to East (from 45 to 25 km, Figure 1, Mauffret et al. [2001]; Nercessian et al. [2001]; Gunnell et al. [2008]; Diaz et al. [2018]; Chevrot et al. [2018]; Wehr et al. [2018]). However, seismic profiles do not highlight major onshore structures in Eastern Pyrénées that could thin the crust as in the Transverse Ranges or in El Emporda basin (the Têt fault seems restricted to the upper half of the crust, Diaz et al. [2018]). The proposed mechanisms to explain this thinning are: 1) the Neogene extension of the crust both in the Eastern Pyrénées and in the North-Catalan Ranges, 2) the retreat of the Tyrrhenian slab and a thermal and mechanical erosion of the lithosphere [Chevrot et al., 2018; Jolivet et al., 2020], and 3) the uplift and erosion of the topography triggered by 1) and 2) and the subsequent lithosphere adjustment [Mauffret et al., 2001; Gunnell et al., 2008; Genti, 2015; Diaz et al., 2018; Wehr et al., 2018]. These processes could be responsible for the transient current stress field in the study area. Further, the deformation described in this article, mainly distributed but also localized along NE–SW and NW–SE faults, could contribute to the crustal thinning. Related to this geodynamic, it is possible that an intrusive magmatic body as recently evidenced by gravimetric and magnetic anomalies along the Catalan Transfer Zone [Canva et al., 2020], could exist bellow the study area. It would be a source of abnormal heat flow at the base of the crust favoring the hydrothermal system.

6 Conclusion

The review of fault motion in the Axial Zone of the Eastern Pyrénées during the Neogene indicates that polymodal fault orientation are inherited from at least three tectonic stages (Hercynian and Pyrenean compression and Oligo-Miocene extension), and has been reactivated since the middle-Miocene. This reactivation period is associated with an increasingly inconsistent body of fault kinematic data, and consequently, a lack of consensus over recent

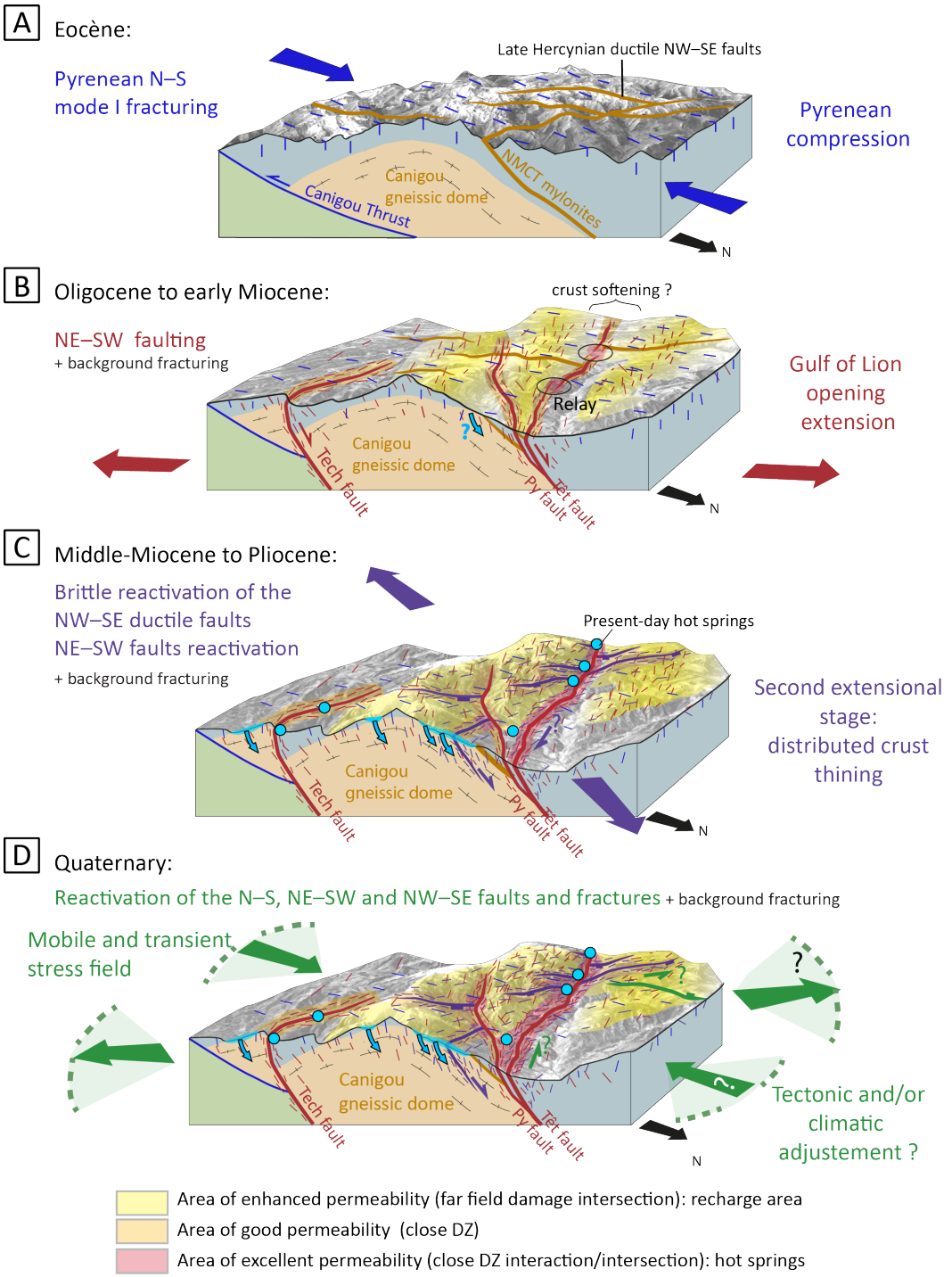

FIGURE 12: Conceptual model of the structural and hydro-geological evolution of the Eastern Pyrénées in relation with the regional tectonics. A) Scattered N–S fractures during the Pyrenean compression. The two following extensional stages (B and C) induce: 1) major fault intersections, providing permeable pathways for fluid upflow, and 2) intersection of secondary fault at high altitude with background fractures, providing permeable infiltration areas for meteoric fluids. The hydrothermal system would have initiated when footwall uplift and fracture intersection make the Canigou-Carança gneissic-dome sufficiently permeable for significant fluid migration at depth, and with sufficient topography convection.

geodynamics, associated with regional uplift and crustal thinning in the Eastern Pyrénées.

The deformation affecting the study area can be split into preferential strike orientations at the regional, secondary fault, and outcrop scale:

1. NW–SE faults (partly inherited from the Hercynian and Pyrenean stages) distributed over the entire study area whose frequency increases towards the Têt fault ;
2. NE–SW faults and fractures formed during the Oligo-Miocene extension of the Gulf of Lion. This deformation is distributed over the study area in the form of secondary faults whose frequency decreases towards the Têt fault.
3. High proportions of N–S fractures and veins, likely formed during the Pyrenean contraction, as a pervasively distributed network.

Additionally, shallow background fracturing related to surface processes (exhumation, topography, glaciation cycles) is widespread.

Intersections of these faults and fractures over recharge areas and at the hot springs provide efficient pathways for meteoric hydrothermal fluids. At the surface, fractures in crystalline rocks have higher average apertures than metasediments. Numerical dislocation models show that the differing mechanical properties of the metasediments and crystalline rocks allow fractures to remain open to a greater depth in the latter than the former. This shows that granites and gneisses are favorable lithologies to enhance hydrothermal fluid flow.

Studying hydro-geothermal systems requires an investigation of the basement fractured reservoir at different scales and depths. This study highlights the challenges of constructing a damage model over regional scale areas in basement environments with polyphased deformation, and calls into question the representativity of single-scale approaches.

7 Acknowledgments

This work was funded by the RGF (Référentiel Géologique de la France) project led by the BRGM (Bureau de Recherche Geologique et Minière), which we thank for its financial and technical support, and supported by the Thermofault project. We sincerely thank

Messrs. Belgrano and Calvet for their huge work of review that have greatly improved the manuscript. The authors wish also to thanks K. Valera, J. Villard, P.Y. Bres, and R. Leroux-Mallouf for their participation to the field campaigns, B. Celerier for his help with the FSA software, Y. Monnier for the statistical analysis, and O. Marc for the language improvement.

References

Ackermann, R. V. and Schlische, R. W. (1997). Anticlustering of small normal faults around larger faults. *Geology*, 25(12) :1127–1130.

Agustí, J., Oms, O., Furió, M., Pérez-Vila, M.-J., and Roca, E. (2006). The messinian terrestrial record in the pyrenees : the case of can vilella (cerdanya basin). *Palaeogeography, Palaeoclimatology, Palaeoecology*, 238(1-4) :179–189.

Anders, M. H. and Wiltschko, D. V. (1994). Microfracturing, paleostress and the growth of faults. *Journal of Structural Geology*, 16(6) :795–815.

Arthaud, F. and Mattauer, M. (1969). Exemples de stylolites d'origine tectonique dans le languedoc, leurs relations avec la tectonique cassante. *Bulletin de la Société géologique de France*, 7(5) :738–744.

Arthaud, F. and Mattauer, M. (1972). Sur l'origine tectonique de certains joints stylolitiques paralleles a la stratification ; leur relation avec une phase de distension (exemple du languedoc). *Bulletin de la Société Géologique de France*, 7(1-5) :12–17.

Arthaud, F. and Pistre, S. (1993). Les fractures et les paléoncontraintes du granite hercynien de millas (zone axiale des pyrénées) : un cas d'étude de la tectonique cassante d'un aquifère de socle. *Geodinamica Acta*, 6(3) :187–201.

Augustinus, P. C. (1995). Glacial valley cross-profile development : the influence of in situ rock stress and rock mass strength, with examples from the southern alps, new zealand. *Geomorphology*, 14(2) :87–97.

Autran, A., Calvet, M., and Delmas, M. (2005). Carte géologique de la france à 1/50 000, feuille mont-louis. *BRGM*.

Aydin, A. (2000). Fractures, faults, and hydrocarbon entrapment, migration and flow. *Marine and petroleum geology*, 17(7) :797–814.

Babault, J. (2004). *Dynamique de l'érosion dans les chaînes de montagnes : Influence de la sédimentation de piedmont. L'exemple des Pyrénées*. PhD thesis.

Baize, S., Cushing, M., Lemeille, F., Granier, T., and Grellet, B. (2002). Inventaire des indices de rupture affectant le quaternaire, en relation avec les grandes structures connues, en france métropolitaine et dans les régions limitrophe. *Mémoires de la Société géologique de France (1924)*, 175 :1–141.

Ballas, G., Soliva, R., Sizun, J.-P., Benedicto, A., Cavailhes, T., and Raynaud, S. (2012). The importance of the degree of cataclasis in shear bands for fluid flow in porous sandstone, provence, france. *AAPG bulletin*, 96(11) :2167–2186.

Banda, E. and Correig, A. (1984). The catalan earthquake of february 2, 1428. *Engineering geology*, 20(1-2) :89–97.

Banks, D., Odling, N. E., Skarphagen, H., and Rohr-Torp, E. (1996). Permeability and stress in crystalline rocks. *Terra Nova*, 8(3) :223–235.

Barton, C. A., Zoback, M. D., and Moos, D. (1995). Fluid flow along potentially active faults in crystalline rock. *Geology*, 23(8) :683–686.

Bartrina, M., Cabrera, L., Jurado, M. J., Guimerà, J., and Roca, E. (1992). Evolution of the central catalan margin of the valencia trough (western mediterranean). *Tectonophysics*, 203(1-4) :219–247.

Belgrano, T. M., Herwegh, M., and Berger, A. (2016). Inherited structural controls on fault geometry, architecture and hydrothermal activity : an example from grimsel pass, switzerland. *Swiss journal of geosciences*, 109(3) :345–364.

Benderitter, Y. and Elsass, P. (1996). Structural control of deep fluid circulation at the soultz hdr site, france : a review. In *International Journal of Rock Mechanics and Mining Sciences and Geomechanics Abstracts*, volume 3, page 104A.

Bense, V., Gleeson, T., Loveless, S., Bour, O., and Scibek, J. (2013). Fault zone hydrogeology. *Earth-Science Reviews*, 127 :171–192.

Bertrand, L. (2016). *Etude des réservoirs géothermiques développés dans le socle et à l'interface avec les formations sédimentaires*. PhD thesis, Université de Lorraine.

Bianchetti, G., Roth, P., Vuataz, F.-D., and Vergain, J. (1992). Deep groundwater circulation in the alps : Relations between water infiltration, induced seismicity and thermal springs. the case of val d'illiez, wallis, switzerland. *Eclogae Geologicae Helvetiae*, 85(2) :291–305.

Bosch, G. V., Van den Driessche, J., Babault, J., Robert, A., Carballo, A., Le Carlier, C., Loget, N., Prognon, C., Wyns, R., and Baudin, T. (2016). Peneplanation and lithosphere dynamics in the pyrenees. *Comptes Rendus Géoscience*, 348(3-4) :194–202.

Bouchez, J. and Gleizes, G. (1995). Two-stage deformation of the mont-louis-andorra granite pluton (variscan pyrenees) inferred from magnetic susceptibility anisotropy. *Journal of the Geological Society*, 152(4) :669–679.

Briais, A., Armijo, R., Winter, T., Tapponnier, P., and Herbecq, A. (1990). Morphological evidence for quaternary normal faulting and seismic hazard in the eastern pyrenees. In *Annales tectonicae*, volume 4, pages 19–42.

Bruhn, R. L., Parry, W. T., Yonkee, W. A., and Thompson, T. (1994). Fracturing and hydrothermal alteration in normal fault zones. *Pure and Applied Geophysics*, 142(3-4) :609–644.

Cabrera, L., Roca, E., and Santanach, P. (1988). Basin formation at the end of a strike-slip fault : the cerdanya basin (eastern pyrenees). *Journal of the Geological Society*, 145(2) :261–268.

Caine, J. S., Bruhn, R. L., and Forster, C. B. (2010). Internal structure, fault rocks, and inferences regarding deformation, fluid flow, and mineralization in the seismogenic stillwater normal fault, dixie valley, nevada. *Journal of Structural Geology*, 32(11) :1576–1589.

Caine, J. S., Evans, J. P., and Forster, C. B. (1996). Fault zone architecture and permeability structure. *Geology*, 24(11) :1025–1028.

Calvet, M. (1999). Régimes des contraintes et volumes de relief dans l'est des pyrénées/stress regimes and volumes of reliefs in the eastern pyrenees. *Géomorphologie : relief, processus, environnement*, 5(3) :253–278.

Calvet, M., Gunnell, Y., and Delmas, M. (2008). Géomorphogenèse des pyrénées. *Pyrénées d'Hier et d'Aujourd'hui, International Year of Planet Earth, TOTAL, BRGM, AGSO, AIPT, CNRS & ed. Atlantica, Biarritz*, pages 129–143.

Calvet, M., Gunnell, Y., and Delmas, M. (2014). The têt river valley : a condensed record of long-term landscape evolution in the pyrenees. In *Landscapes and Landforms of France*, pages 127–138. Springer.

Calvet, P. (1996). Morphogenèse d'une montagne méditerranéenne, les pyrénées orientales (vol. 1, 1170 p). *Paris : University of Paris.*

Campbell, K. A., Rodgers, K., Brotheridge, J. M., and Browne, P. (2002). An unusual modern silica–carbonate sinter from pavlova spring, ngatamariki, new zealand. *Sedimentology*, 49(4) :835–854.

Cantarero, I., Alías, G., Cruset, D., Carola, E., Lanari, P., and Travé, A. (2018). Fluid composition changes in crystalline basement rocks from ductile to brittle regimes. *Global and planetary change*, 171 :273–292.

Cantarero, I., Lanari, P., Vidal, O., Alías, G., Travé, A., and Baqués, V. (2014). Long-term fluid circulation in extensional faults in the central catalan coastal ranges : P–t

constraints from neoformed chlorite and k-white mica. *International Journal of Earth Sciences*, 103(1) :165–188.

Canva, A., Thinon, I., Peyrefitte, A., Couëffé, R., Maillard, A., Jolivet, L., Martelet, G., Lacquement, F., and Guennoc, P. (2020). The catalan magnetic anomaly : Its significance for the crustal structure of the gulf of lion passive margin and relationship to the catalan transfer zone. *Marine and Petroleum Geology*, 113 :104174.

Carlsson, A. and Olsson, T. (1982). High rock stresses as a consequence of glaciation. *Nature*, 298(5876) :739.

Carozza, J.-M. and Baize, S. (2004). L'escarpement de faille de la têt est-il le résultat de la tectonique active plio-pléistocène ou d'une exhumation pléistocène ? *Comptes Rendus Géoscience*, 336(3) :217–226.

Carozza, J.-M. and Delcaillau, B. (1999). L'enregistrement géomorphologique de la tectonique quaternaire par les nappes alluviales : l'exemple du bassin de la têt (roussillon, france). *Comptes Rendus de l'Académie des Sciences-Series IIA-Earth and Planetary Science*, 329(10) :735–740.

Carozza, J.-M. and Delcaillau, B. (2000). Réponse des bassins versants à l'activité tectonique : l'exemple de la terminaison orientale de la chaîne pyrénéenne. approche morphotectonique/ drainage basins response to active tectonics : example from eastern pyrenees. morphotectonic approach. *Géomorphologie : relief, processus, environnement*, 6(1) :45–60.

Casas, T. (1984). *Estudi de la deformació en els gneis del massís del Canigó*. Universitat de Barcelona.

Chéry, J., Zoback, M. D., and Hassani, R. (2001). An integrated mechanical model of the san andreas fault in central and northern california. *Journal of Geophysical Research : Solid Earth*, 106(B10) :22051–22066.

Chester, F. and Logan, J. (1986). Implications for mechanical properties of brittle faults from observations of the punchbowl fault zone, california. *Pure and Applied Geophysics*, 124(1-2) :79–106.

Chevrot, S., Sylvander, M., and Delouis, B. (2011). A preliminary catalog of moment tensors for the pyrenees. *Tectonophysics*, 510(1-2) :239–251.

Chevrot, S., Sylvander, M., Diaz, J., Martin, R., Mouthereau, F., Manatschal, G., Masini, E., Calassou, S., Grimaud, F., Pauchet, H., et al. (2018). The non-cylindrical crustal architecture of the pyrenees. *Scientific reports*, 8(1) :9591.

Choukroune, P., Seguret, M., and Galdeano, A. (1973). Caracteristiques et evolution structurale des pyrenees ; un modele de relations entre zone orogenique et mouvement des plaques. *Bulletin de la Société géologique de France*, 7(5-6) :600–611.

Clark, C. D. and Wilson, C. (1994). Spatial analysis of lineaments. *Computers & Geosciences*, 20(7-8) :1237–1258.

Clarke, B. A. and Burbank, D. W. (2011). Quantifying bedrock-fracture patterns within the shallow subsurface : Implications for rock mass strength, bedrock landslides, and erodibility. *Journal of Geophysical Research : Earth Surface*, 116(F4).

Clauzon, G. (1987). Le détritisme néogène du bassin du roussillon (pyrénées-orientales, france). *Geologie Alpine Mem.*, hs n.13 :427–441.

Clauzon, G., Le Strat, P., Duvail, C., Do Couto, D., Suc, J.-P., Molliex, S., Bache, F., Besson, D., Lindsay, E. H., Opdyke, N. D., et al. (2015). The roussillon basin (s. france) : A case-study to distinguish local and regional events between 6 and 3 ma. *Marine and Petroleum Geology*, 66 :18–40.

Cointre, M. (1987). Etude neotectonique des pyrénées orientales. Technical report.

Cox, S. C., Menzies, C. D., Sutherland, R., Denys, P. H., Chamberlain, C., and Teagle, D. A. (2015). Changes in hot spring temperature and hydrogeology of the alpine fault hanging wall, new zealand, induced by distal south island earthquakes. *Geofluids*, 15(1-2) :216–239.

Curewitz, D. and Karson, J. A. (1997). Structural settings of hydrothermal outflow : Fracture permeability maintained by fault propagation and interaction. *Journal of Volcanology and Geothermal Research*, 79(3) :149–168.

Curry, M. E., Van Der Beek, P., Huismans, R. S., Wolf, S., and Muñoz, J. A. (2019). Peak- to post-orogenic landscape evolution of the pyrenees mountains from numerical modeling and thermochronology. *AGUFM*, 2019 :T41G–0339.

De Joussineau, G., Bazalgette, L., Petit, J.-P., and Lopez, M. (2005). Morphology, intersections, and syn/late-diagenetic origin of vein networks in pelites of the lodève permian basin, southern france. *Journal of Structural Geology*, 27(1) :67–87.

Delcaillau, B., Carozza, J.-M., and Font, M. (2004). Le segment nord de la faille de la têt (pyrénées-orientales) : fonctionnement néogène et implications géomorphologiques. *Bulletin Société Géologique de France*, (3) :257–272.

Delmas, M., Calvet, M., Gunnell, Y., Voinchet, P., Manel, C., Braucher, R., Tissoux, H., Bahain, J.-J., Perrenoud, C., Saos, T., et al. (2018). Terrestrial 10be and electron spin

resonance dating of fluvial terraces quantifies quaternary tectonic uplift gradients in the eastern pyrenees. *Quaternary Science Reviews*, 193 :188–211.

Diamond, L. W., Wanner, C., and Waber, H. N. (2018). Penetration depth of meteoric water in orogenic geothermal systems. *Geology*, 46(12) :1063–1066.

Diaz, J., Vergés, J., Chevrot, S., Antonio-Vigil, A., Ruiz, M., Sylvander, M., and Gallart, J. (2018). Mapping the crustal structure beneath the eastern pyrenees. *Tectonophysics*, 744 :296–309.

Donville, B. (1973a). Ages potassium-argon des roches volcaniques de la dépression de la selva (nord-est de l'espagne). *CR Acad. Sci. Paris*, 277 :1–4.

Donville, B. (1973b). *Géologie néogene et âges des eruptions volcaniques de la Catalogne Orientale*. PhD thesis.

Duvail, C., Gorini, C., Lofi, J., Le Strat, P., Clauzon, G., and dos Reis, A. T. (2005). Correlation between onshore and offshore pliocene–quaternary systems tracts below the roussillon basin (eastern pyrenees, france). *Marine and Petroleum Geology*, 22(6-7) :747–756.

Earnest, E. and Boutt, D. (2014). Investigating the role of hydromechanical coupling on flow and transport in shallow fractured-rock aquifers. *Hydrogeology journal*, 22(7) :1573–1591.

Faillat, J., Aguilar, J.-P., Calvet, M., and Michaux, J. (1990). Les fissures à remplissages fossilifères néogènes du plateau de baixas (pyrénées-orientales, france), témoins de la distension oligo-miocène. *Comptes Rendus de l'Académie des Sciences de Paris II*, 311 :205–212.

Faulds, J., Coolbaugh, M., Bouchot, V., Moek, I., and Oguz, K. (2010). Characterizing structural controls of geothermal reservoirs in the great basin, usa, and western turkey : Developing successful exploration strategies in extended terranes. In *World Geothermal Congress 2010*, pages 11–p.

Faulkner, D., Jackson, C., Lunn, R., Schlische, R., Shipton, Z., Wibberley, C., and Withjack, M. (2010). A review of recent developments concerning the structure, mechanics and fluid flow properties of fault zones. *Journal of Structural Geology*, 32(11) :1557–1575.

Faulkner, D., Mitchell, T., Healy, D., and Heap, M. (2006). Slip on 'weak' faults by the rotation of regional stress in the fracture damage zone. *Nature*, 444(7121) :922–925.

Fleta, J., Santanach, P., Goula, X., Martinez, P., Grellet, B., and Masana, E. (2001). Preliminary geologic, geomorphologic and geophysical studies for the paleoseismological analysis of the amer fault (ne spain). *Geologie En Mijnbouw*, 80(3/4) :243–254.

Forster, C. and Smith, L. (1989). The influence of groundwater flow on thermal regimes in mountainous terrain : a model study. *Journal of Geophysical Research : Solid Earth*, 94(B7) :9439–9451.

Forster, C. B., Caine, J. S., Schulz, S., and Nielson, D. L. (1997). Fault zone architecture and fluid flow an example from dixie valley, nevada. In *Proceedings, Twenty-second Workshop on Geothermal Reservoir Engineering, Stanford University, Stanford, California*, pages 123–130.

Fossen, H. (2016). *Structural geology*. Cambridge University Press.

Gabrielsen, R. H. and Braathen, A. (2014). Models of fracture lineaments—joint swarms, fracture corridors and faults in crystalline rocks, and their genetic relations. *Tectonophysics*, 628 :26–44.

Genti, M. (2015). *Impact des processus de surface sur la déformation actuelle des Pyrénées et des Alpes*. PhD thesis, Université de Montpellier.

Géraud, Y., Diraison, M., and Orellana, N. (2006). Fault zone geometry of a mature active normal fault : a potential high permeability channel (pirgaki fault, corinth rift, greece). *Tectonophysics*, 426(1) :61–76.

Goula, X., Olivera, C., Fleta, J., Grellet, B., Lindo, R., Rivera, L., Cisternas, A., and Carbon, D. (1999). Present and recent stress regime in the eastern part of the pyrenees. *Tectonophysics*, 308(4) :487–502.

Gourinard, Y. (1971). Determination cartographique et geophysique des failles bordières du fossé neogene de cerdagne - pyrenees orientales franco-epagnoles. *96em Congres National des Sciences Savantes, Toulouse 1971*, pages 245–263.

Guimerà i Rosso, J. J. (1988). *Estudi estructural de l'enllaç entre la Serralada Ibèrica i la Serralada Costanera Catalana*. Universitat de Barcelona.

Guitard, G., Geyssant, J., Laumonier, B., Autran, A., Fonteilles, M., Dalmayrac, B., Vidal, J., and Bandet, Y. (1992). Carte géol. france (1/50 000), feuille prades (1095).

Guitard, G., Laumonier, B., Autran, A., Bandet, Y., and Berger, G. (1998). Notice explicative, carte géologique france (1 : 50.000), feuille prades (1095). *BRGM, Orléans*.

Gunnell, Y., Calvet, M., Brichau, S., Carter, A., Aguilar, J.-P., and Zeyen, H. (2009). Low long-term erosion rates in high-energy mountain belts : insights from thermo-and biochronology in the eastern pyrenees. *Earth and Planetary Science Letters*, 278(3-4) :208–218.

Gunnell, Y., Zeyen, H., and Calvet, M. (2008). Geophysical evidence of a missing lithospheric root beneath the eastern pyrenees : Consequences for post-orogenic uplift and associated geomorphic signatures. *Earth and Planetary Science Letters*, 276(3-4) :302–313.

Gupta, A. and Scholz, C. H. (2000). A model of normal fault interaction based on observations and theory. *Journal of Structural Geology*, 22(7) :865–879.

Hasenmueller, E. A., Gu, X., Weitzman, J. N., Adams, T. S., Stinchcomb, G. E., Eissenstat, D. M., Drohan, P. J., Brantley, S. L., and Kaye, J. P. (2017). Weathering of rock to regolith : The activity of deep roots in bedrock fractures. *Geoderma*, 300 :11–31.

Hatheway, A. and Kiersch, G. (1989). Engineering properties of rock. *Practical Handbook of Physical Properties of Rocks and Minerals*, pages 672–715.

Howald, T., Person, M., Campbell, A., Lueth, V., Hofstra, A., Sweetkind, D., Gable, C. W., Banerjee, A., Luijendijk, E., Crossey, L., et al. (2015). Evidence for long timescale (> 103 years) changes in hydrothermal activity induced by seismic events. *Geofluids*, 15(1-2) :252–268.

Huyghe, D., Mouthereau, F., Segalen, L., and Furió, M. (2020). Long-term dynamic topographic support during post-orogenic crustal thinning revealed by stable isotope (d18 o) paleo-altimetry in eastern pyrenees. *Scientific reports*, 10(1) :1–8.

Ingebritsen, S. and Manning, C. (1999). Geological implications of a permeability-depth curve for the continental crust. *Geology*, 27(12) :1107–1110.

Ingebritsen, S. and Manning, C. (2010). Permeability of the continental crust : dynamic variations inferred from seismicity and metamorphism. *Geofluids*, 10(1-2) :193–205.

Ishii, E. (2016). Far-field stress dependency of the failure mode of damage-zone fractures in fault zones : Results from laboratory tests and field observations of siliceous mudstone. *Journal of Geophysical Research : Solid Earth*, 121(1) :70–91.

Jarman, D., Calvet, M., Corominas, J., Delmas, M., and Gunnell, Y. (2014). Large-scale rock slope failures in the eastern pyrenees : Identifying a sparse but significant population in paraglacial and parafluvial contexts. *Geografiska Annaler : Series A, Physical Geography*, 96(3) :357–391.

Jolivet, L., Romagny, A., Gorini, C., Maillard, A., Thinon, I., Couëffé, R., Ducoux, M., and Seranne, M. (2020). Fast dismantling of a mountain belt by mantle flow : Late-orogenic evolution of pyrenees and liguro-provençal rifting. *Tectonophysics*, 776 :228312.

Jordan, G. and Schott, B. (2005). Application of wavelet analysis to the study of spatial pattern of morphotectonic lineaments in digital terrain models. a case study. *Remote Sensing of Environment*, 94(1) :31–38.

Kattenhorn, S. A., Aydin, A., and Pollard, D. D. (2000). Joints at high angles to normal fault strike : an explanation using 3-d numerical models of fault-perturbed stress fields. *Journal of structural Geology*, 22(1) :1–23.

Kattenhorn, S. A. and Pollard, D. D. (2001). Integrating 3-d seismic data, field analogs, and mechanical models in the analysis of segmented normal faults in the wytch farm oil field, southern england, united kingdom. *AAPG bulletin*, 85(7) :1183–1210.

Kim, Y.-S., Andrews, J. R., and Sanderson, D. J. (2001). Reactivated strike–slip faults : examples from north cornwall, uk. *Tectonophysics*, 340(3-4) :173–194.

King, G. C., Stein, R. S., and Lin, J. (1994). Static stress changes and the triggering of earthquakes. *Bulletin of the Seismological Society of America*, 84(3) :935–953.

Krimissa, M. (1995). *Application des méthodes isotopiques à l'étude des eaux thermales en milieu granitique (Pyrénées, France)*. PhD thesis, Université Paris XI.

Lacan, P. and Ortuño, M. (2012). Active tectonics of the pyrenees : A review. *Journal Of Iberian Geology, 2012, vol. 38, num. 1, p. 9-30.*

Laubach, S. E., Lamarche, J., Gauthier, B. D., Dunne, W. M., and Sanderson, D. J. (2018). Spatial arrangement of faults and opening-mode fractures. *Journal of Structural Geology*, 108 :2–15.

Laumonier, B., Calvet, M., Delmas, M., Barbey, P., Lenoble, J., and Autran, A. (2017). Notice explicative Carte géologique de la France à 1/50 000, feuille Mont-Louis (1094). *Orléans : BRGM*, page 139 3 pl. ht.

Laumonier, B., Calvet, M., Le Bayon, B., Barbey, P., and Lenoble, J.-L. (2015a). avec la collaboration de Cocherie A., Melleton J. – Notice explicative, Carte géologique de la France à 1/50 000, feuille Prats-de-Mollo-la-Preste (1099). *Orléans : BRGM. Carte géologique par Laumonier B., Le Bayon B., Calvet M.*, page 189.

Laumonier, B., Le Bayon, B., and Calvet, M. (2015b). Carte géologique de la France à 1/50 000, feuille Prats-de-Mollo-la-Preste (1099). *Orléans : BRGM. Notice explicative par Laumonier B., Calvet M., LeBayon B., Barbey P., Lenoble J.-L.*, page 189.

Leclerc, J., Bellier, O., Sebrier, M., and Calvet, M. (2001). Variations du champ de contrainte cenozoique et deformations récentes du bassin du roussillon. *Le Quaternaire des Pyrénées orientales dans son cadre géomorphologique.–Livret guide de l'excursion annuelle de l'Association francaise pour l'Etude du Quaternaire.*

Leith, K., Moore, J. R., Amann, F., and Loew, S. (2014a). In situ stress control on microcrack generation and macroscopic extensional fracture in exhuming bedrock. *Journal of Geophysical Research : Solid Earth*, 119(1) :594–615.

Leith, K., Moore, J. R., Amann, F., and Loew, S. (2014b). Subglacial extensional fracture development and implications for alpine valley evolution. *Journal of Geophysical Research : Earth Surface*, 119(1) :62–81.

Lewis, C. J., Vergés, J., and Marzo, M. (2000). High mountains in a zone of extended crust : Insights into the neogene-quaternary topographic development of northeastern iberia. *Tectonics*, 19(1) :86–102.

Llac, F. (1989). Notice explicative, Carte géologique de la France à 1/50 000, feuille Saillagouse (1099). *Orléans : BRGM. Carte géologique par Llac, F., Autran, A., Guitard, G., Robert, J.F., Gourinard, Y., Santanach, P. (1988).*

Llac, F., Autran, A., Guitard, G., Robert, J., Gourinard, Y., and Santanach, P. (1988). Carte géologique de la France à 1/50 000, feuille Saillagouse (1098). *Orléans : BRGM. Notice explicative par Llac F. (1989).*

López, D. L. and Smith, L. (1995). Fluid flow in fault zones : analysis of the interplay of convective circulation and topographically driven groundwater flow. *Water Resources Research*, 31(6) :1489–1503.

Lowell, R. P., Van Cappellen, P., and Germanovich, L. N. (1993). Silica precipitation in fractures and the evolution of permeability in hydrothermal upflow zones. *Science-New-York then Washington*, 260 :192–192.

Luby, S., Geraud, Y., Diraison, M., Wicker, M., Bertrand, L., and Bossennec, C. (2020). Multi-scale investigation focusing on the lineament of the pan-african basement (eastern egypt). In *Fourth Naturally Fractured Reservoir Workshop*, volume 2020, pages 1–5. European Association of Geoscientists & Engineers.

Maerten, F., Maerten, L., and Pollard, D. D. (2014). ibem3d, a three-dimensional iterative boundary element method using angular dislocations for modeling geologic structures. *Computers & Geosciences*, 72 :1–17.

Magri, F., Möller, S., Inbar, N., Möller, P., Raggad, M., Rödiger, T., Rosenthal, E., and Siebert, C. (2016). 2d and 3d coexisting modes of thermal convection in fractured hydrothermal systems-implications for transboundary flow in the lower yarmouk gorge. *Marine and Petroleum Geology*, 78 :750–758.

Marrett, R., Gale, J. F., Gómez, L. A., and Laubach, S. E. (2018). Correlation analysis of fracture arrangement in space. *Journal of Structural Geology*, 108 :16–33.

Mauffret, A., de Grossouvre, B. D., Dos Reis, A. T., Gorini, C., and Nercessian, A. (2001). Structural geometry in the eastern pyrenees and western gulf of lion (western mediterranean). *Journal of Structural Geology*, 23(11) :1701–1726.

Maurel, O. (2003). *L'exhumation de la Zone Axiale des Pyrenees orientales : Une approche thermo-chronologique multi-methodes du role des failles.* PhD thesis, Université Montpellier II.

Maurel, O., Brunel, M., and Monie, P. (2002). Exhumation cenozoique des massifs du canigou et de mont-louis (pyrenees orientales, france). *Comptes Rendus Geoscience*, 334(12) :941–948.

Maurel, O., Monnier, P., Pik, R., Arnaud, N., Brunel, M., and Jolivet, M. (2008). The meso-cenozoic thermo-tectonic evolution of the eastern pyrenees : an 40 ar/39 ar fission track and (u-th)/he thermochronological study of the canigou and mont-louis massifs. *International Journal of Earth Sciences*, 97(3) :565–584.

Mayolle, S., Soliva, R., Caniven, Y., Wibberley, C., Ballas, G., Milesi, G., and Dominguez, S. (2019). Scaling of fault damage zones in carbonate rocks. *Journal of Structural Geology*, 124 :35–50.

Mazurek, M. (2000). Geological and hydraulic properties of water-conducting features in crystalline rocks. In *Hydrogeology of crystalline rocks*, pages 3–26. Springer.

McCaig, A. and Miller, J. (1986). 40ar-39ar age of mylonites along the merens fault, central pyrenees. *Tectonophysics*, 129(1-4) :149–172.

Medialdea, T., Vázquez, J., and Vegas, R. (1994). Estructura y evolución geodinámica del extremo noreste del margen continental catalán durante el neógeno. *Acta geológica hispánica*, 29(2-4) :39–53.

Meixner, J., Grimmer, J., Becker, A., Schill, E., and Kohl, T. (2018). Comparison of different digital elevation models and satellite imagery for lineament analysis : Implications for identification and spatial arrangement of fault zones in crystalline basement rocks of the southern black forest (germany). *Journal of Structural Geology*, 108 :256–268.

Milesi, G. (2020). *Analyse thermochronologique, géochimique et structurale du système hydrothermal de la faille de la Têt (Pyrénées, France), un nouvel outil d'exploration géothermique.* PhD thesis, Université de Montpellier.

Milesi, G., Monié, P., Münch, P., Soliva, R., Taillefer, A., Bruguier, O., Bellanger, M., Bonno, M., and Martin, C. (2020). Tracking geothermal anomalies along a crustal fault using (u-th)/ he apatite thermochronology and rare-earth element (ree) analyses : the example of the têt fault (pyrenees, france). *Solid Earth*, 11(5) :1747–1771.

Milesi, G., Soliva, R., Monié, P., Münch, P., Bellanger, M., Bruguier, O., Bonno, M., Taillefer, A., and Mayolle, S. (2019). Mapping a geothermal anomaly using apatite (u-th)/he thermochronology in the têt fault damage zone, eastern pyrenees, france. *Terra Nova*, 31(6) :569–576.

Mitchell, T. and Faulkner, D. (2009). The nature and origin of off-fault damage surrounding strike-slip fault zones with a wide range of displacements : a field study from the atacama fault system, northern chile. *Journal of Structural Geology*, 31(8) :802–816.

Moeck, I. S. (2014). Catalog of geothermal play types based on geologic controls. *Renewable and Sustainable Energy Reviews*, 37 :867–882.

Mynatt, I., Seyum, S., and Pollard, D. D. (2009). Fracture initiation, development, and reactivation in folded sedimentary rocks at raplee ridge, ut. *Journal of Structural Geology*, 31(10) :1100–1113.

Nercessian, A., Mauffret, A., Dos Reis, A., Vidal, R., Gallart, J., and Diaz, J. (2001). Deep reflection seismic images of the crustal thinning in the eastern pyrenees and western gulf of lion. *Journal of Geodynamics*, 31(2) :211–225.

Norton, D. and Knapp, R. (1977). Transport phenomena in hydrothermal systems : the nature of porosity. *Am. J. Sci. ;(United States)*, 277.

Novakova, L. and Pavlis, T. L. (2017). Assessment of the precision of smart phones and tablets for measurement of planar orientations : A case study. *Journal of Structural Geology*, 97 :93–103.

Oele, E., Sluiter, J., and Pannekoek, A. (1963). Tertiary and quaternary sedimentation in the conflent. *An intramontane rift valley in the Eastern Pyrenees. Leidse. Geol. Meded*, 28 :297–319.

Olivera, C. (2006). *Els terratrèmols dels segles XIV i XV a Catalunya*, volume 30. Generalitat de Catalunya, Institut Cartogràfic de Catalunya.

Peacock, D., Nixon, C., Rotevatn, A., Sanderson, D., and Zuluaga, L. (2016). Glossary of fault and other fracture networks. *Journal of Structural Geology*, 92 :12–29.

Perea, H. (2009). The catalan seismic crisis (1427 and 1428 ; ne iberian peninsula) : geological sources and earthquake triggering. *Journal of Geodynamics*, 47(5) :259–270.

Person, M., Hofstra, A., Sweetkind, D., Stone, W., Cohen, D., Gable, C., and Banerjee, A. (2012). Analytical and numerical models of hydrothermal fluid flow at fault intersections. *Geofluids*, 12(4) :312–326.

Petit, C. and Mouthereau, F. (2012). Steep topographic slope preservation by anisotropic diffusion : An example from the neogene têt fault scarp, eastern pyrenees. *Geomorphology*, 171 :173–179.

Philip, H. (2018). *Tectonique récente et actuelle, in : Synthèse géophysique et géologique des Pyrénées - Volume 3 : Cycle alpin : Phénomènes alpins*. BRGM/AGSO.

Philip, H., Bousquet, J.-C., Escuer, J., Fleta, J., Goula, X., and Grellet, B. (1992). Présence de failles inverses d'âge quaternaire dans l'est des pyrénées : implications sismotectoniques. *Comptes rendus de l'Académie des sciences. Série 2, Mécanique, Physique, Chimie, Sciences de l'univers, Sciences de la Terre*, 314(11) :1239–1245.

Pous, J., Julià, R., and Sugrañes, L. S. (1986). Cerdanya basin geometry and its implication on the neocene evolution of the eastern pyrenees. *Tectonophysics*, 129(1-4) :355–365.

Pyrak-Nolte, L. and Morris, J. (2000). Single fractures under normal stress : The relation between fracture specific stiffness and fluid flow. *International Journal of Rock Mechanics and Mining Sciences*, 37(1) :245–262.

Ranjram, M., Gleeson, T., and Luijendijk, E. (2015). Is the permeability of crystalline rock in the shallow crust related to depth, lithology or tectonic setting ? *Geofluids*, 15(1-2) :106–119.

Rehault, J., Moussat, E., and Fabbri, A. (1987). Structural evolution of the tyrrhenian back-arc basin. *Marine Geology*, 74(1-2) :123–150.

Renard, F., Gratier, J.-P., and Jamtveit, B. (2000). Kinetics of crack-sealing, intergranular pressure solution, and compaction around active faults. *Journal of Structural Geology*, 22(10) :1395–1407.

Rigo, A., Vernant, P., Feigl, K., Goula, X., Khazaradze, G., Talaya, J., Morel, L., Nicolas, J., Baize, S., Chery, J., et al. (2015). Present-day deformation of the pyrenees revealed by gps surveying and earthquake focal mechanisms until 2011. *Geophysical Journal International*, 201(2) :947–964.

Roca, E. and Desegaulx, P. (1992). Analysis of the geological evolution and vertical movements in the valencia trough area, western mediterranean. *Marine and Petroleum Geology*, 9(2) :167–176.

Roure, F., Choukroune, P., Berastegui, X., Munoz, J., Villien, A., Matheron, P., Bareyt, M., Seguret, M., Camara, P., and Deramond, J. (1989). Ecors deep seismic data and balanced cross sections : Geometric constraints on the evolution of the pyrenees. *Tectonics*, 8(1) :41–50.

Saar, M. and Manga, M. (2004). Depth dependence of permeability in the oregon cascades inferred from hydrogeologic, thermal, seismic, and magmatic modeling constraints. *Journal of Geophysical Research : Solid Earth*, 109(B4).

Sander, P., Minor, T. B., and Chesley, M. M. (1997). Ground-water exploration based on lineament analysis and reproducibility tests. *Groundwater*, 35(5) :888–894.

Sanderson, D. J. (2016). Field-based structural studies as analogues to sub-surface reservoirs. *Geological Society, London, Special Publications*, 436(1) :207–217.

Sanderson, D. J. and Kim, Y.-S. (2005). The relationship between displacement and length of faults. *Earth-Science Reviews*, 68(3-4) :317–334.

Saula, E., Picart, J., Mató, E., Llenas, M., Losantos, M., Berástegui, X., and Agustí, J. (1994). Evolución geodinámica de la fosa del empordà y las sierras transversales. *Acta geológica hispánica*, 29(2-4) :55–75.

Sausse, J. (1998). *Caractérisation et modélisation des écoulements fluides en milieu fissuré. Relation avec les altérations hydrothermales et quantification des paléocontraintes.* PhD thesis, Université Henri Poincaré-Nancy I.

Savage, H. M. and Brodsky, E. E. (2011). Collateral damage : Evolution with displacement of fracture distribution and secondary fault strands in fault damage zones. *Journal of Geophysical Research : Solid Earth*, 116(B3).

Schneeberger, R., Egli, D., Lanyon, G. W., Mäder, U. K., Berger, A., Kober, F., and Herwegh, M. (2018). Structural-permeability favorability in crystalline rocks and implications for groundwater flow paths : a case study from the aar massif (central switzerland). *Hydrogeology Journal*, 26(8) :2725–2738.

Séranne, M. (1999). The gulf of lion continental margin (nw mediterranean) revisited by ibs : an overview. *Geological Society, London, Special Publications*, 156(1) :15–36.

Séranne, M., Benedicto, A., Labaum, P., Truffert, C., and Pascal, G. (1995). Structural style and evolution of the gulf of lion oligo-miocene rifting : Role of the pyrenean orogeny. *Marine and Petroleum geology*, 12(8) :809–820.

Sibson, R. (1977). Fault rocks and fault mechanisms. *Journal of the Geological Society*, 133(3) :191–213.

Sibson, R. H. (1987). Earthquake rupturing as a mineralizing agent in hydrothermal systems. *Geology*, 15(8) :701–704.

Smith, D. J., Jenkin, G., Petterson, M., Naden, J., Fielder, S., Toba, T., and Chenery, S. (2011). Unusual mixed silica–carbonate deposits from magmatic–hydrothermal hot springs, savo, solomon islands. *Journal of the Geological Society*, 168(6) :1297–1310.

Snow, D. T. (1968). Rock fracture spacings, openings, and porosities. *Journal of Soil Mechanics & Foundations Div.*

Sonney, R. and Vuataz, F.-D. (2009). Numerical modelling of alpine deep flow systems : a management and prediction tool for an exploited geothermal reservoir (lavey-les-bains, switzerland). *Hydrogeology Journal*, 17(3) :601–616.

Souriau, A. and Pauchet, H. (1998). A new synthesis of pyrenean seismicity and its tectonic implications. *Tectonophysics*, 290(3) :221–244.

Steer, P., Bigot, A., Cattin, R., and Soliva, R. (2011). In-situ characterization of the effective elasticity of a fault zone, and its relationship to fracture spacing. *Journal of Structural Geology*, 33(11) :1541–1553.

Stober, I. and Bucher, K. (1999). Deep groundwater in the crystalline basement of the black forest region. *Applied geochemistry*, 14(2) :237–254.

Stober, I. and Bucher, K. (2007). Hydraulic properties of the crystalline basement. *Hydrogeology Journal*, 15(2) :213–224.

Stober, I. and Bucher, K. (2015). Hydraulic conductivity of fractured upper crust : insights from hydraulic tests in boreholes and fluid-rock interaction in crystalline basement rocks. *Geofluids*, 15(1-2) :161–178.

Suc, J.-P. and Fauquette, S. (2012). The use of pollen floras as a tool to estimate palaeoaltitude of mountains : The eastern pyrenees in the late neogene, a case study. *Palaeogeography, Palaeoclimatology, Palaeoecology*, 321 :41–54.

Taillefer, A., Guillou-Frottier, L., Soliva, R., Magri, F., Lopez, S., Courrioux, G., Millot, R., Ladouche, B., and Le Goff, E. (2018). Topographic and faults control of hydrothermal circulation along dormant faults in an orogen. *Geochemistry, Geophysics, Geosystems*, 19(12) :4972–4995.

Taillefer, A., Soliva, R., Guillou-Frottier, L., Le Goff, E., Martin, G., and Seranne, M. (2017). Fault-related controls on upward hydrothermal flow : an integrated geological study of the têt fault system, eastern pyrénées (france). *Geofluids*, 2017.

Tassone, A. A., Roca, E., Muñoz, J., Cabrera, L., and Artigas, M. C. (1994). Evolución del sector septentrional del margen continental catalán durante el cenozoico. *Acta geológica hispánica*, 29(2) :3–37.

Tavani, S., Granado, P., Corradetti, A., Seers, T., and Muñoz, J. A. (2020). Transverse jointing in foreland fold-and-thrust belts : a remote sensing analysis in the eastern pyrenees. *Solid Earth Discussions*, pages 1–20.

Ternois, S., Odlum, M., Ford, M., Pik, R., Stockli, D., Tibari, B., Vacherat, A., and Bernard, V. (2019). Thermochronological evidence of early orogenesis, eastern pyrenees, france. *Tectonics*, 38(4) :1308–1336.

Turu, V. and Planas, X. (2005). Inestabilidad de vertientes en los valles del valira. datos y dataciones para el establecimiento de una cronología, posibles causas. andorra y alt urgell (pirineos orientales). In *VI Simposio Nacional sobre Taludes y Laderas Inestables. Valencia, Abstracts*.

Vignaroli, G., Pinton, A., De Benedetti, A. A., Giordano, G., Rossetti, F., Soligo, M., and Berardi, G. (2013). Structural compartmentalisation of a geothermal system, the torre alfina field (central italy). *Tectonophysics*, 608 :482–498.

Wang, Q., Laubach, S., Gale, J., and Ramos, M. (2019). Quantified fracture (joint) clustering in archean basement, wyoming : application of the normalized correlation count method. *Petroleum Geoscience*, 25(4) :415–428.

Wanner, C., Waber, H. N., and Bucher, K. (2020). Geochemical evidence for regional and long-term topography-driven groundwater flow in an orogenic crystalline basement (aar massif, switzerland). *Journal of hydrology*, 581 :124374.

Wehr, H., Chevrot, S., Courrioux, G., and Guillen, A. (2018). A three-dimensional model of the pyrenees and their foreland basins from geological and gravimetric data. *Tectonophysics*, 734 :16–32.

Wibberley, C. A., Yielding, G., and Di Toro, G. (2008). Recent advances in the understanding of fault zone internal structure : a review. *Geological Society, London, Special Publications*, 299(1) :5–33.

Yeats, R. S., Sieh, K. E., Allen, C. R., and Geist, E. (1997). *The geology of earthquakes*, volume 568. Oxford university press New York.